Inference of Cirrus Cloud Properties Using Satellite-observed Visible and Infrared Radiances. Part I: Parameterization of Radiance Fields

PATRICK MINNIS

Atmospheric Sciences Division, NASA Langley Research Center, Hampton, Virginia

KUO-NAN LIOU AND YOSHIHIDE TAKANO

Department of Meteorology, University of Utah, Salt Lake City, Utah

(Manuscript received 3 January 1992, in final form 20 July 1992)

ABSTRACT

Current techniques for deriving cirrus optical depth and altitude from visible (0.65 μm) and infrared (11.5 μm) satellite data use radiative transfer calculations based on scattering phase functions of spherical water droplets. This study examines the impact of using phase functions for spherical droplets and hexagonal ice crystals to analyze radiances from cirrus. Adding–doubling radiative transfer calculations are used to compute radiances for different cloud thicknesses and heights over various backgrounds. These radiances are used to develop parameterizations of top-of-the-atmosphere visible reflectance and infrared emittance utilizing tables of reflectance as a function of cloud optical depth, viewing and illumination angles, and microphysics. This parameterization, which includes Rayleigh scattering, ozone absorption, variable cloud height, and an anisotropic surface reflectance, reproduces the computed top-of-the-atmosphere reflectances with an accuracy of ±6% for four microphysical models: 10-μm water droplet, small symmetric crystal, cirrostratus, and cirrus uncinus. The accuracy is twice that of previous models.

Bidirectional reflectance patterns from theoretical ice-crystal clouds are distinctly different from those of the theoretical water-droplet clouds. In general, the ice-crystal phase functions produce significantly larger reflectances than the water-droplet phase function for a given optical depth. A parameterization relating infrared emittance to visible optical depth is also developed. The effective infrared emittances computed with the adding–doubling method are reproduced with a precision of ±2%. Infrared scattering reduces emittance by an average of 5%. Simulated cloud retrievals using the parameterization indicate that optical depths and cloud temperatures can be determined with an accuracy of ~25% and ~6 K for typical cirrus conditions. Retrievals of colder clouds over brighter surfaces are not as accurate, while those of warmer clouds over dark surfaces will be more reliable. Sensitivity analyses show that the use of the water-droplet phase function to interpret radiances from a theoretical cirrostratus cloud will significantly overestimate the optical depth and underestimate cloud height by 1.5–2.0 km for nominal cirrus clouds (temperature of 240 K and visible optical depth of ~1). The parameterization developed here is economical in terms of computer memory and is useful for both simulation and interpretation of cloud radiance fields.

1. Introduction

Accurate quantification of cirrus cloud properties from satellite measurements is particularly important to understanding the role of cirrus in climate change. In addition to their effects on the atmospheric energy budget through latent heat exchanges, high altitude ice clouds significantly modulate the flow of radiative energy into and out of the earth–atmosphere system. The influence of cirrus clouds on climate has been discussed extensively by Liou (1986). One of the main topics stressed by that review paper was the need for more research of the radiative properties and distribution of cirrus.

Corresponding author address: Dr. Patrick Minnis, NASA Langley Research Center, Mail Stop 420, 21 Ames Rd., Hampton, VA 23681-5225.

Cirrus clouds are strong absorbers at infrared wavelengths. Due to their relatively small optical depths, however, only part of the radiation emitted from lower levels and from the earth's surface is absorbed by cirrus clouds. Emission of longwave radiation by these clouds takes place at temperatures less than those of the surface and lower levels. Thus, depending on the cloud's optical thickness and altitude, the combined transmitted and emitted radiation lost to space in the presence of cirrus clouds can be considerably less than that from the clear sky. This radiation "trapping" effect results in longwave warming of the surface and troposphere. The additional tropospheric heating, mainly confined to the upper layers, has a significant influence on the general circulation. For example, it may cause acceleration of the subtropical jets and strengthening of the tropical precipitation maxima (Slingo and Slingo 1988).

Interaction of cirrus with solar radiation is primarily

dominated by scattering. Because of small optical depths and the scattering properties of large ice crystals, the albedo of cirrus tends to be relatively low. Thus, while cirrus clouds reflect some of the incoming solar radiation, the amount of shortwave cooling of the surface–troposphere system due to cloud shading is generally less than that for most water clouds. The albedo of thicker cirrus clouds, however, may be sufficient to block solar warming of the surface with significant impact on local and, perhaps, larger-scale circulations.

The overall effect (e.g., cooling or warming) of cirrus on the energy balance of the earth–atmosphere system depends on the areal coverage, optical depths, altitudes, and horizontal locations of the clouds. In order to realistically include the effects of cirrus and other clouds in climate models—typically, general circulation models—the global distribution of these variables must be correctly computed through parameterizations of physical cloud processes. Knowledge of the climatological distribution of these quantities is critical to the development and validation of parameterizations of cloud cover in climate models.

One of the goals of the International Satellite Cloud Climatology Project (ISCCP; see Schiffer and Rossow 1983) is to provide a reliable cloud climatology for climate model validation. To that end, the ISCCP is making an ambitious effort to derive global cloud parameters on a 3-hourly basis using various satellites over an extended time period. During the daytime, cloud amounts, altitudes, and optical depths are included among the list of derived quantities. The ISCCP analysis algorithm (Rossow et al. 1988) relies entirely on bispectral data taken at visible (VIS, $\sim$0.65 μm) and infrared (IR, $\sim$11.5 μm) wavelengths.

Some of the earliest attempts to determine cloud fraction from VIS and IR data used simple methods applied to unispectral data (e.g., Arking 1964). Schenk and Curran (1973) and Reynolds and Vonder Haar (1977) briefly explored the use of VIS–IR bispectral techniques to determine bulk cirrus properties. The development and application of their methods, however, was only cursory. Platt et al. (1980) utilized similar ideas in a case study employing geostationary satellite data and surface lidar measurements. Their approach is incorporated in the analyses and parameterizations developed here. Coakley and Bretherton (1982) developed an IR method to explicitly account for partially cloud-filled pixels based on spatial variability of the radiance field. Their technique relied on the assumption of blackbody clouds. Minnis and Harrison (1984) and Minnis et al. (1987) conceived and applied a variable threshold, bispectral technique that has been shown to provide reliable values of cloud fractional coverage (e.g., Minnis and Wielicki 1988) over the complete diurnal cycle. Their results also rely on the black-cloud assumption resulting in uncertain cloud heights for nonblack clouds. Arking and Childs (1985) constructed a clustering algorithm that utilizes VIS and IR data together with radiances in the 3.7-μm spectral region to estimate the cloud optical depth and microphysical model. That approach does not adjust cloud height for small optical depths and requires three sensors. With the development of microwave and other thermal infrared radiometers, it was found that cirrus cloud heights could be estimated more accurately than with available VIS–IR methods. These techniques, which use atmospheric sounding channels (e.g., Smith et al. 1970; Chahine 1974; Wielicki and Coakley 1981; Yeh and Liou 1983), are unable to separate cloud fraction from cloud emittance and are unreliable for the detection of low-level clouds. A few other techniques have been examined using other channels (e.g., Wu 1985), but like the sounding-channel techniques, these methods have limited applicability because of their relatively sparse temporal coverage of the earth. Only VIS and IR sensors are common to all operational geostationary and polar orbiting weather satellites. Thus, for full, consistent, global monitoring of clouds over all times of day, it is essential to use a technique that relies solely on VIS and IR data. This spectral commonality provides part of the motivation for use of a VIS–IR method by the ISCCP. The importance of VIS–IR-derived cloud cover to climate studies necessitates a thorough examination and subsequent improvement of the ISCCP analysis techniques.

The basic premise for using the bispectral approach to account for nonblack clouds is that the VIS extinction coefficient is related to the IR absorption coefficient. This relationship implies that the cloud VIS reflectance may be used to infer the cloud IR emittance. Having a value for the clear-sky IR radiance, it is possible to correct the observed cloudy radiance for cloud emittance to obtain an estimate of the radiance emanating from some specified level in the cloud. The equivalent blackbody temperature of this level, usually the center or top of the cloud, is converted to cloud altitude by means of a vertical sounding. The critical relationship ultimately required for this approach is the dependence of IR emittance on VIS reflectance through the IR and VIS optical depths. Since clouds scatter radiation anisotropically, this relationship is also influenced by the viewing and illumination conditions.

The ISCCP cirrus analysis (Rossow et al. 1988) utilizes a combination of theoretical and empirical models to determine the cloud visible optical depth from the observed reflectance, the cloud emittance from the visible optical depth, and, finally, the cloud-top temperature from the cloud emittance and the observed infrared radiance. The ISCCP theoretical cloud radiative model consists of an unwieldy set of lookup tables relating top-of-the-atmosphere reflectance to VIS cloud optical depth as functions of viewing and illumination angles, surface albedo, and cloud height. The ISCCP lookup tables summarize the results of extensive radiative transfer computations that simulated the scattering and absorption by water droplet clouds embed-

ded in a Rayleigh-scattering atmosphere over two types of reflecting surfaces: Lambertian for land, snow, and ice and anisotropic over water. The cloud droplets are described with a modified gamma size distribution having an effective radius of 10 μm and an effective variance of 0.10. Thus, the ISCCP scheme assumes that all clouds have the radiative properties of this particular model cloud.

Cloud IR emittance is determined from the ISCCP VIS cloud optical depth using Beer's law for transmission through a medium. The IR absorption optical depth is given by the VIS optical depth divided by the scattering efficiency ratio, the ratio of the VIS scattering efficiency to the IR absorption efficiency. For water droplets of this size, the value of the ratio of VIS scattering efficiency to infrared absorption efficiency, or scattering efficiency ratio, is approximately 2.4. An analysis of coincident satellite and lidar data by Platt et al. (1980) and theoretical calculations assuming cylindrical-shaped ice crystals (Platt 1979) suggest that this ratio is approximately equal to 2.0 for cirrus. The ISCCP algorithm utilizes the latter value of the scattering efficiency ratio to provide a link between the water droplet model and actual cirrus clouds. An empirical study by Minnis et al. (1990b) found that the ratio is closer to 2.1 for cirrus clouds.

Cirrus clouds are primarily composed of ice crystals with various shapes having maximum dimensions ranging from about 20 to 2000 μm (e.g., Heymsfield and Platt 1984). The scattering properties of hexagonal ice crystals differ considerably from spherical particles (Liou 1986). Because of the complexities involved in computing scattering by hexagonal solids, cylindrical columns were initially used to approximate hexagonal crystals in radiative transfer calculations (e.g., Liou 1973). More recently, Takano and Liou (1989a) have employed ray-tracing techniques to compute scattering patterns for simple ice crystals in the form of hexagonal plates and columns of various dimensions. Their results are the most realistic to date in that they reproduce certain well-known cirrus optical phenomena.

From these and other studies (Platt 1973; Platt and Dilley 1979; Paltridge and Platt 1981; Platt 1983; Platt and Dilley 1984; Platt et al. 1987), it appears that:

1) cirrus cloud scattering properties are similar to those of hexagonal crystals, resulting in reflectance patterns unlike those from spheres, and
2) the value of the scattering efficiency ratio is between 1.8 and 4.0.

The full impact of these features on cirrus properties derived using a VIS–IR bispectral retrieval is unknown. Differences between ice-crystal and water-droplet bidirectional reflectance patterns will introduce errors into the retrieved VIS optical depth. Uncertainties in the scattering efficiency ratio may cause significant errors in the estimation of IR optical depth with subsequent errors in the vertical location of the cloud.

This paper examines the relationship between VIS reflectance and IR emittance for deriving cirrus parameters from satellite data. The two primary goals of this effort are:

1) development and examination of a bispectral cloud parameter retrieval algorithm that incorporates variable cloud microphysics, and
2) evaluation of the ISCCP algorithm and model for determining cirrus height and optical depth.

Part I develops a model that parameterizes reflected and emitted radiances computed with the adding–doubling method of radiative transfer. This parameterization forms the basis of the retrieval algorithm. The primary variables of interest are the cloud altitude and optical depth. Part II (Minnis et al. 1993) uses several datasets taken during the First ISCCP Regional Experiment (FIRE) Cirrus Intensive Field Observations (IFO; see Starr 1987) to test the new algorithm. The ISCCP technique is also simulated and tested.

In Part I, theoretical calculations are performed to estimate the bidirectional reflectance fields as functions of cloud optical depth and particle shape and size. The computations use scattering phase functions derived from Mie theory for spherical particles and from geometric ray tracing for hexagonal crystals (Takano and Liou 1989a). Results from the calculations are used to develop a parameterization of top-of-the-atmosphere reflectance based on the cloud's altitude, optical depth, and microphysics and the reflectance properties of the underlying surface. This parameterization incorporates lookup tables that relate cloud reflectance to cloud microphysics and optical depth. VIS optical depth for a given particle category is determined by matching the calculated with the satellite-observed reflectances. Radiative transfer computations using the corresponding IR phase functions are used to develop a parameterization of cloud emittance based on the VIS optical depth. Cloud temperature and altitude are adjusted with this emittance parameterization using the measurement of VIS optical depth. The sensitivity of the derived cloud temperature to the cloud microphysical model is also explored. These results provide a theoretical estimate of the uncertainties of the ISCCP algorithm's capabilities for determining cirrus cloud-top height and optical depth from VIS and IR radiances measured by meteorological satellites.

2. Radiative transfer model

The detection of a cloud and subsequent quantification of its bulk physical properties rely on measurements of radiance or specific intensity. Consider a plane-parallel layer of the atmosphere. Neglecting the wavelength indexing for simplicity, the intensity, I, of a beam of radiation propagating in the direction Ω through a medium having the optical depth τ may be

described with the general equation of radiative transfer as follows:

$$\mu \frac{dI(\tau, \Omega)}{d\tau} = I(\tau, \Omega) - J(\tau, \Omega), \qquad (1)$$

where Ω is defined by the azimuth angle ϕ and by μ, the cosine of the zenith angle θ. The source function is denoted by J.

There is only scattering in the visible spectral interval so that the source function is

$$J(\tau; \mu, \phi) = \frac{\tilde{\omega}}{4\pi} \int_0^{2\pi} \int_{-1}^{1} I(\tau; \mu', \phi') P(\mu, \phi; \mu', \phi') d\mu' d\phi' + \frac{\tilde{\omega}}{4\pi} F_\odot P(\mu, \phi; -\mu_\odot, \phi_\odot) \exp(-\tau/\mu_\odot),$$

where $F_\odot$ is the incoming solar irradiance, $\mu_\odot$ is the cosine of the solar zenith angle $\theta_\odot$, $\tilde{\omega}$ is the single-scattering albedo, and P is the single-scattering phase function. The zenith angles of the incident and outgoing beams are θ' and θ, respectively. Their respective cosines are μ' and μ. Similarly, the azimuth angles of the incoming and outgoing beams are ϕ' and ϕ, respectively. Thus, the incident direction is given by (μ', ϕ') in the case of multiple scattering or by $(-\mu_\odot, \phi_\odot)$ in the case of direct solar radiation, and (μ, ϕ) defines the outgoing direction. Downward directions are denoted with a minus sign. The scattering geometry shown in Fig. 1 defines the scattering angle Θ.

In the IR, emission is an important source term. Azimuthal dependence of the scattering is neglected because of the emissive nature of the earth and atmosphere. Thus, the IR source function is

$$J(\tau, \mu) = \frac{\tilde{\omega}}{2} \int_{-1}^{1} I(\tau, \mu') P(\mu, \mu') d\mu' + (1 - \tilde{\omega}) B(T),$$

where the first term represents the contribution of multiple scattering and the second term describes the emission of the layer at temperature T.

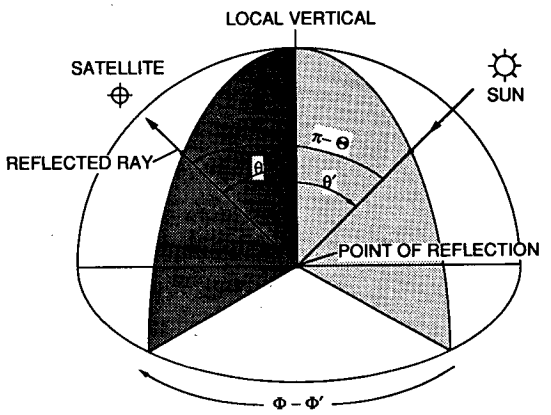

FIG. 1. Sun–satellite scattering geometry.

To make an inference about a cloud based on a measurement of I above the atmosphere, it is necessary to account for the attenuation of the radiation by both the atmosphere and the cloud. Thus, (1) must be solved for a multilayer, multiple scattering system. The adding–doubling method is used here to solve (1) for a three-layer atmosphere over a purely reflecting or emitting surface. Although this method for radiative transfer has been described in detail elsewhere (e.g., Lacis and Hansen 1974; Liou 1980; Takano and Liou 1989b), it is briefly reviewed here to document the incorporation of the emission source function in its formulation.

The adding–doubling method makes use of the reflection function R, the transmission function T, and the emission source function J_e. The first two variables are defined in terms of the radiation incident from either the top or bottom of some arbitrary horizontally homogeneous layer characterized by a single-scattering albedo, phase function, and optical depth. The second term of the IR source function depends only on the temperature and single-scattering albedo.

1) FORMULATION FOR VISIBLE WAVELENGTHS

For radiance incident from above, the intensities emergent from the top and bottom of a layer are defined by

$$I_{\text{out,top}}(\mu, \phi) = \frac{1}{\pi} \int_0^{2\pi} \int_0^{1} R(\mu, \phi; \mu', \phi') \times I_{\text{in,top}}(\mu', \phi') \mu' d\mu' d\phi', \qquad (2a)$$

$$I_{\text{out,bottom}}(\mu, \phi) = \frac{1}{\pi} \int_0^{2\pi} \int_0^{1} T(\mu, \phi; \mu', \phi') \times I_{\text{in,top}}(\mu', \phi') \mu' d\mu' d\phi'. \qquad (2b)$$

For radiance incident from below, the intensities are as follows:

$$I_{\text{out,bottom}}(\mu, \phi) = \frac{1}{\pi} \int_0^{2\pi} \int_0^{1} R^*(\mu, \phi; \mu', \phi') \times I_{\text{in,bottom}}(\mu', \phi') \mu' d\mu' d\phi', \qquad (3a)$$

$$I_{\text{out,top}}(\mu, \phi) = \frac{1}{\pi} \int_0^{2\pi} \int_0^{1} T^*(\mu, \phi; \mu', \phi') \times I_{\text{in,bottom}}(\mu', \phi') \mu' d\mu' d\phi', \qquad (3b)$$

where the asterisk superscript indicates that the incident radiation comes from below the layer. For the VIS, the intensity incident at the top of the atmosphere is

$$I_{\text{in,top}}(-\mu_o, \phi_o) = I_o(\mu', \phi') = \delta(\mu' - \mu_o)\delta(\phi' - \phi_o)F_o,$$

where δ is Dirac delta function.

The reflection and transmission functions can be derived analytically from (2) and (3) by using the single-scattering approximation in (1) and solving for R and T. If an infinitesimal layer is considered such that $\Delta\tau = 10^{-8}$, that is, $\Delta\tau \to 0$, then

$$R(\mu, \mu_o; \phi - \phi_o) = \frac{\Delta\tau}{4\mu\mu_o}\tilde{\omega}P(\mu, -\mu_o; \phi - \phi_o), \quad (4)$$

$$T(\mu, \mu_o; \phi - \phi_o) = \frac{\Delta\tau}{4\mu\mu_o}\tilde{\omega}P(-\mu, -\mu_o; \phi - \phi_o). \quad (5)$$

Similarly, it can be shown that $R^* = R$ and $T^* = T$ for a thin homogeneous layer. When two or more layers are added together to obtain new reflection and transmission functions, R^* and T will not necessarily be equal to R and T^*, respectively.

Now consider two stacked layers denoted by subscripts 1 and 2 with optical depths, τ_1 and τ_2. The reflection and total transmission functions R_{12} and $\tilde{T}_{12}$ for the combined layers can be determined by following the conventional adding principle for radiative transfer (e.g., Lacis and Hansen 1974; Liou 1980). That procedure is described with the following equations:

$$Q = R_1^* R_2, \quad (6a)$$

$$S = Q(1 - Q)^{-1}, \quad (6b)$$

$$D = T_1 + ST_1 + S\exp(-\tau_1/\mu_o), \quad (6c)$$

$$D = D + \exp(-\tau_1/\mu_o), \quad (6d)$$

$$U = R_2 D + R_2\exp(-\tau_1/\mu_o), \quad (6e)$$

$$T_{12} = D\exp(-\tau_2/\mu) + T_2\exp(-\tau_1/\mu_o) + T_2 D, \quad (6f)$$

$$\tilde{T}_{12} = T_{12} + \exp\left[-\left(\frac{\tau_1}{\mu_o} + \frac{\tau_2}{\mu}\right)\right]\delta(\mu - \mu_o), \quad (6g)$$

$$R_{12} = R_1 + \exp(-\tau_1/\mu_o)U + T_1^* U. \quad (6h)$$

The parameters lacking the tilde indicate diffuse components only. The product of two functions in this system of equations implies an integration over the appropriate solid angle to account for all possible multiple-scattering contributions. For example,

$$R_1^* R_2 = \frac{1}{\pi}\int_0^{2\pi}\int_0^1 R_1^*(\mu, \phi; \mu', \phi') \times R_2(\mu', \phi'; \mu_o, \phi_o)\mu' d\mu' d\phi'.$$

This integration is performed using Gaussian quadrature with each multiplication taking place at a given Gaussian point.

A similar system of equations can be solved to determine R and T^* for the combined layers for radiation from below as follows:

$$Q = R_2 R_1^*, \quad (7a)$$

$$S = Q(1 - Q)^{-1}, \quad (7b)$$

$$U = ST_2^* + T_2^* + S\exp(-\tau_2/\mu'), \quad (7c)$$

$$D = R_1^* U + R_1^*\exp(-\tau_2/\mu'), \quad (7d)$$

$$T_{12}^* = U\exp(-\tau_1/\mu) + UT_1^* + T_1^*\exp(-\tau_2/\mu'), \quad (7e)$$

$$R_{12}^* = R_2^* + \exp(-\tau_2/\mu)D + T_2 D. \quad (7f)$$

The reflection and transmission functions are computed for a homogeneous layer with optical depth τ in the following manner. A starting optical depth $\Delta\tau$ is selected such that $\Delta\tau \approx 10^{-8}$. To minimize the number of computations, $\tau_1 = \tau_2 = \Delta\tau$ in the beginning. Equations (6) and (7) are solved in sequence to obtain R and T for the combined layers with optical depth $2\Delta\tau$. The process is repeated n times using the new values of R, R^*, T, and T^* and $\tau_1 = \tau_2$ each time. The final values of the reflection and transmission functions correspond to those for a layer with optical depth τ. This procedure constitutes the doubling method.

For an inhomogeneous atmosphere containing N different homogeneous layers, consider the diagram in Fig. 2. The value for R_{top} is computed for the whole atmosphere by cumulatively combining the different homogeneous layers, l, with (6) and (7) from the top down to the surface. If a surface is included, it is treated as layer $N+1$ with $T_{N+1} = 0$. For a Lambertian surface, $R_{N+1} = \alpha_g$, the surface albedo. Otherwise, $R = \rho_g(\mu_o, \mu, \phi - \phi_o)$, the surface bidirectional reflectance.

In the application of this method, the phase functions used in (4) and (5) are expanded numerically in Legendre polynomials using a Fourier expansion in the azimuthal direction. The form of the expansion is

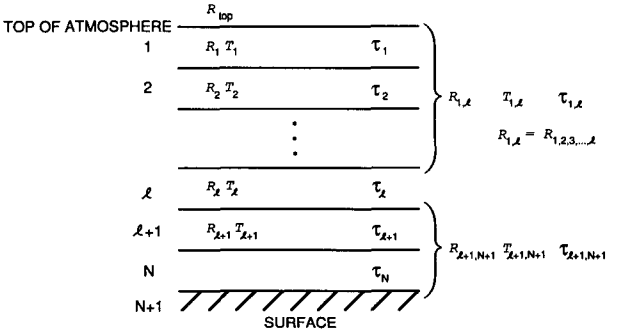

FIG. 2. Schematic diagram of atmospheric layers for application of adding method for radiative transfer.

$$P(\mu, \mu'; \phi - \phi') = \sum_{m=0}^{M} \sum_{l=m}^{M} \tilde{\omega}_l^m P_l^m(\mu) P_l^m(\mu') \cos m(\phi - \phi'),$$

where

$$\tilde{\omega}_l^m = (2 - \delta_{0,m}) \tilde{\omega}_l \frac{(l-m)!}{(l+m)!} (l = m, \cdots, M), \quad 0 \leq m \leq M,$$

$$\delta_{0,m} = \begin{cases} 1, & \text{if } m = 0 \\ 0, & \text{otherwise;} \end{cases}$$

P_l^m denote the associated Legendre polynomials, and M is the number of Fourier expansion coefficients.

Before expansion, the phase functions are truncated following the procedures outlined by Takano and Liou (1989b). The truncated fraction to account for diffraction is $f \approx 0.5$ in the limit of geometric optics. The optical depth and single-scattering albedo are adjusted for the truncation using the similarity principle, where

$$\tau' = \tau_s' + \tau_a = (1 - f\tilde{\omega})\tau$$

and

$$\tilde{\omega}' = \frac{\tau_s'}{\tau'} = \frac{(1-f)\tilde{\omega}}{1 - f\tilde{\omega}},$$

respectively. The phase function does not account for plane-parallel transmission through the particle that is referred to as δ-transmission (Takano and Liou 1989a). The optical thickness and single-scattering albedos must be further adjusted using the same procedures as above such that

$$\tau'' = (1 - f_\delta \tilde{\omega}')\tau'$$

and

$$\tilde{\omega}'' = \frac{(1 - f_\delta)\tilde{\omega}'}{1 - f_\delta \tilde{\omega}'},$$

where f_δ is the fraction of the incident radiation that passes directly through the particle. Thus, following Takano and Liou (1989a), the fraction of radiation effectively scattered in the forward direction is

$$f_D = \frac{1}{2\tilde{\omega}(1 - f_\delta)}.$$

2) FORMULATION FOR INFRARED WAVELENGTHS

At infrared wavelengths, the adding principle is adapted to account for emission. For a thin layer having the optical thickness $\Delta\tau \approx 10^{-8}$, the upward and downward emission in the emergent direction, μ, may be given by

$$J^+(\mu) = J^-(-\mu) \approx (1 - \tilde{\omega})B(T)\Delta\tau/\mu,$$

where the superscripts $^+$ and $^-$ denote radiation emitted in the upward and downward directions from the layer, respectively. The upward and downward source terms at the interface of layers 1 and 2 are expressed by

$$J_d = [1 + R_1^* R_2 + (R_1^* R_2)^2 + \cdots]J_1^- + [1 + R_1^* R_2 + (R_1^* R_2)^2 + \cdots]R_1^* J_2^+ = (1 + S)(J_1^- + R_1^* J_2^+),$$

and

$$J_u = [1 + R_2^* R_1 + (R_2^* R_1)^2 + \cdots]J_2^+ + [1 + R_2^* R_1 + (R_2^* R_1)^2 + \cdots]R_2 J_1^- = (1 + S^*)(J_2^+ + R_2 J_1^-).$$

The multiple reflection terms S and S^* are given by (6b) and (7b), respectively.

The upward and downward emission source terms at the top and bottom of the combined layer are simply

$$J_{12}^+ = J_1^+ + \tilde{T}_1^* J_u$$

and

$$J_{12}^- = J_2^- + \tilde{T}_2 J_d,$$

respectively, where the total transmission, $\tilde{T}$, is the sum of the diffuse, T, and the direct components as follows:

$$\tilde{T} = T + \exp(-\tau/\mu).$$

As in the case for solar radiation, the reflection and diffuse transmission functions are the same for radiation from below and above a homogeneous layer. The initial reflection and diffuse transmission functions are computed in the same manner as in (4) and (5), except that μ_0 is replaced by μ' and no azimuth term is included. Homogeneous layers are added in the same fashion as before beginning with the boundary conditions such that the surface transmittance is zero, the surface emission is treated as a separate layer with the emission only going upward, and the radiance incident at the top of the atmosphere is zero.

3. Parameterizations of cloud reflectance

The two parameters of primary interest in the interpretation of satellite measurements are the optical depth and altitude (pressure level or height) of the cloud. The latter is derived from cloud temperature—the radiatively important parameter at IR wavelengths. The former can be derived from VIS data. Methods are needed to account for the various noncloud processes contributing to the observed radiance, however, in order to isolate the radiance due solely to the cloud itself. Once the cloud radiance is determined, the optical depth may be estimated from the results of the adding–doubling calculations. Using the adding–doubling method directly to match the observed radiance on any operational basis is computationally prohibitive.

Therefore, parameterized versions of the more complex radiative transfer models are developed to enable the determination of the cloud optical depth and emittance economically from the satellite data.

Minnis et al. (1990a) enhanced a simple parameterization originally given by Platt et al. (1980) to derive cloud optical depth from satellite-measured VIS reflectance over high cirrus clouds. That parameterization is further generalized here in order to improve high-level cloud retrievals and to allow for the interpretation of lower-level cloud reflectance.

a. Formulation

Consider the two-level, plane-parallel atmosphere depicted on the left side of Fig. 3. In clear skies, the reflectance, $\rho = \rho_s$, measured by the satellite results from absorption and scattering within the atmosphere and from reflection by the surface. In the schematic (Fig. 3) depicting this process, diffuse scattering is denoted with multiple arrows and nonprimary direct scattering is denoted with multiple reflections of a given beam off a horizontal line. The radiance entering the top layer is first diminished by absorption according to Beer's Law for the optical depth τ_{a1}. The radiation beam then enters the first Rayleigh layer with scattering optical depth, τ_{R1}. This beam is scattered by the molecules giving rise to a reflectance ρ_{R1} exiting the top of the layer in the direction of the satellite. Both aerosol and Rayleigh scattering may occur within the bottom layer giving rise to another reflectance ρ_{R2} at the top layer. Another fraction, the surface reflectance ρ_g, of the combined attenuated direct beam and the downwelling diffuse irradiance resulting from scattering is reflected back to the top layer. The measured reflectance, in this case

$$\rho = \rho_s = \pi I_{\odot}\uparrow(\mu_{\odot}, \mu, \psi)/F_{\odot}\mu_{\odot}, \tag{8}$$

is a function of these three reflectances diminished by the absorption during both ingression and egression of the beam. The subscript $\odot$ refers to the sun. For the remainder of this text, the solar and viewing zenith angles will be represented by $\theta_{\odot}$ and θ with their respective cosines denoted by $\mu_{\odot}$ and μ. The azimuth angle relative to the sun is given by $\psi = \phi - \phi_{\odot}$.

Insertion of a cloud layer with VIS optical depth τ_v, shown on the right side of Fig. 3, complicates this picture considerably. The radiation that passes through the top layers is reflected by the cloud or passes through the cloud either unattenuated as a direct beam or diffusely after multiple scattering. The reflected radiance then undergoes additional scattering and absorption by the top layers as it exits the top of the atmosphere. Thus, the reflectance contributed by the cloud and the atmosphere above it is

$$\rho_1 = T_{a1}\rho_{c1} = T_{a1}\rho_{c1}(\tau_v, \tau_{R1}), \tag{9}$$

where the transmittance,

$$T_{a1} = \exp[-\tau_{a1}(1/\mu_{\odot} + 1/\mu)],$$

accounts for the ozone absorption and ρ_{c1} is a parameterization of the reflectance of the combined Rayleigh and cloud layers. The ozone-absorption optical depth is

$$\tau_{a1} = u(0.085 - 0.00052u)$$

(Inn and Tanaka 1953; Rossow et al. 1988), where u is the ozone path length (cm-STP). The cloud reflectance,

$$\rho_c = \pi I_c\uparrow(\tau_v, \mu_{\odot}, \mu, \psi)/F_c\downarrow,$$

where the subscript c refers to the radiation at the top of the cloud, F is the irradiance, and the downward arrow indicates incidence at the cloud top.

The reflectance due to radiation unaffected by the presence of the cloud is approximated by

$$\rho_2 = T_c\downarrow T_c\uparrow \rho_s, \tag{10}$$

where the cloud transmittances are

$$T_c\downarrow = \exp[-(1 - f_D)\tau_v/\mu_{\odot}] \tag{11}$$

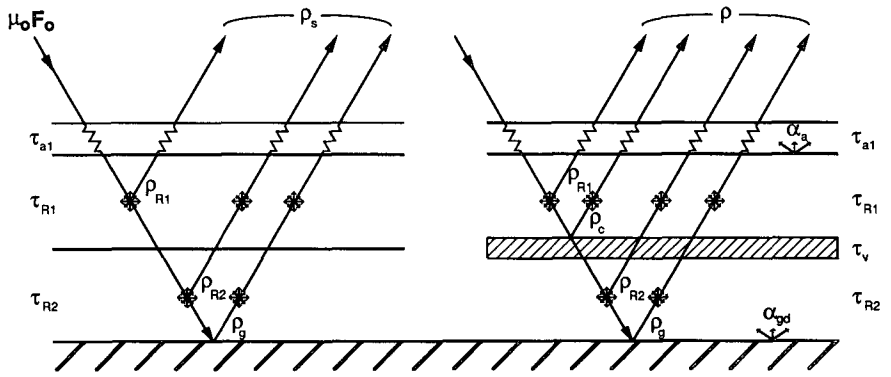

FIG. 3. Schematic diagram of scattering and absorption processes for a three-layer atmosphere with no clouds (left) and with one cloud layer (right).

and

$$T_c\uparrow = \exp[-(1 - f_D)\tau_v/\mu]. \quad (12)$$

The proportion of the radiation scattered out of the forward direction, reflected by the surface, and transmitted diffusely back through the cloud to space is approximated as

$$\rho_3 = \alpha_{sd}(1 - \alpha_{cd})(1 - T_c\uparrow - \alpha_c). \quad (13)$$

Cloud albedo is $\alpha_c(\tau_v, \mu_\odot) = F_c\uparrow/F_c\downarrow$. In terms of cloud reflectance,

$$\alpha_c = \frac{1}{\pi}\int_0^{2\pi}\int_0^1 \rho_c(\tau, \mu_\odot, \mu, \psi)\mu d\psi d\mu.$$

The diffuse cloud albedo is

$$\alpha_{cd}(\tau_v) = 2\int_0^1 \alpha_c(\tau_v, \mu_\odot)\mu_\odot d\mu_\odot.$$

The diffuse clear-sky albedo is

$$\alpha_{sd} = 2\int_0^1 \alpha_s(\mu_\odot)\mu_\odot d\mu_\odot,$$

where the clear-sky albedo is

$$\alpha_s = \frac{1}{\pi}\int_0^{2\pi}\int_0^1 \rho_s(\mu_\odot, \mu, \psi)\mu d\psi d\mu.$$

Combining (9), (10), and (13) yields an approximation of the measured reflectance,

$$\rho = \rho_1 + \rho_2 + \rho_3. \quad (14)$$

This equation reduces to (8) when clouds are absent. It goes beyond the parameterization of Minnis et al. (1990a) by including Rayleigh scattering above the cloud and by accounting for the effects of variable particle size on the magnitude of the forward-scattered component.

b. *Cloud reflectance computations*

The cloud reflectance, albedo, and diffuse albedo used in (14) can be computed using the adding–doubling model described above. In this study, values for these parameters were calculated with the radiative transfer model using four different scattering phase functions. A phase function derived from Mie-scattering computations for water droplets having a modified gamma size distribution with an effective radius of 10 μm and an effective variance of 0.05 is used to calculate a τ–ρ_c relationship equivalent to that used by the ISCCP. All references to this phase function are denoted as WD. The WD droplet size distribution has an effective variance that is only half that of the one used by the ISCCP. The WD model is equivalent to the ISCCP model; however, since the single-scattering albedos are the same, the phase functions are nearly identical, and the asymmetry factors differ by only 0.1%. A monodisperse phase function for randomly oriented hexagonal ice crystals having equal diameter, $2a$, and length, L, of 20 μm (C20) is used to represent small crystals, while the cirrostratus (CS) and cirrus uncinus (CU) phase functions given by Takano and Liou (1989a) are used to represent size distributions equivalent to midsize ($L/2a \approx 85$ μm/40 μm) and large ($L/2a \approx 400$ μm/120 μm) ice crystals, respectively.

These scattering phase functions are plotted in Fig. 4 for $\lambda = 0.55$ μm. The scattering properties of ice crystals and water droplets at 0.55 μm are essentially the same as those at 0.65 μm. The shape of the WD curve is typical of the phase function for the sizes of water droplets found in the atmosphere. A well-defined minimum occurs in the side-scattering directions between $\Theta = 90°$ and 120°, a rainbow feature is seen near $\Theta = 140°$, a glory occurs near $\Theta = 180°$, and a relatively strong maximum exists in the forward-scattering direction. All three ice-crystal phase functions have similar shapes but different magnitudes. In general, they are less anisotropic than the WD with side scattering comparable in magnitude to backscattering. The forward-scattering peaks are greater than that for the WD. Instead of a smoothly varying increase of scattering probability from 90° to 0°, the ice-crystal phase functions show three discontinuous peaks. These maxima correspond to inner and outer halos at 22° and 46°, respectively, and to the diffraction and transmission maxima superimposed at $\Theta = 0°$. The slight relative maximum near 156° is displaced by more than 15° from the WD rainbow feature. The number of scattering features unique to either ice or WD suggest that there should be significant differences in the reflectance patterns of ice and water-droplet clouds.

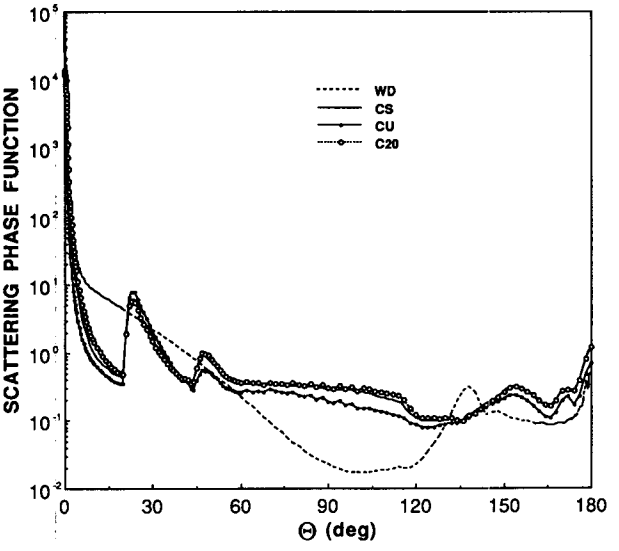

FIG. 4. Scattering phase functions for various cloud particle size distributions, $\lambda = 0.55$ μm.

TABLE 1. Optical properties of model clouds.

Cloud type	VIS parameters				IR parameters	
	$\tilde{\omega}$	f_δ	f_D	g	$\tilde{\omega}$	g
WD	1.0000	0.000	0.500	0.8725	0.5292	0.9325
C20	1.0000	0.120	0.568	0.7704	0.5784	0.9116
CS	1.0000	0.126	0.572	0.7824	0.5528	0.9405
CU	1.0000	0.155	0.592	0.8404	0.5330	0.9686

Utilization of these phase functions in the adding–doubling calculations requires values for the forward-scattering fraction and $\tilde{\omega}$. The values from Takano and Liou (1989a), listed in Table 1, are used here. For all spherical particles, $f_\delta = 0$ and $f_D = 0.5$ in the limit of geometric optics. The single-scattering albedo for $\lambda = 0.55$ μm is actually 0.999999 for all four particles. The phase functions were expanded using 120 and 100 Fourier coefficients and 330 and 200 Legendre polynomials for the ice-crystal and WD computations, respectively. The integrals over zenith angle were solved using Gaussian quadrature with 40 emergent angles given by their cosines.

The adding–doubling calculations were performed for $\tau_v = 0.25$, 0.5, 1, 2, 3, 4, 8, and 16 for all four phase functions. Additional computations were performed for $\tau_v = 32$ and 64 for the WD model. The results were interpolated to create lookup tables of ρ_c, α_c, and α_{cd} for $\mu_\odot = 0.05, 0.15, \cdots, 0.95, 1.0$; $\mu = 0, 0.1, 0.2, \cdots, 1.0$; and $\psi = 0°, 5°, 15°, 30°, \cdots, 165°, 175°, 180°$. Linear interpolation in $\mu_\odot$, μ, τ_v, and ψ is used to find values of ρ_c, α_c, and α_{cd} for a particular set of angles and optical depth.

Results of these calculations for cloud albedo are shown in Fig. 5 for several optical depths. In general, the WD albedos are substantially lower than all of the other models for a given optical depth. There is almost a 100% difference in the albedos between the WD and C20 models at $\tau = 1$ and 4 for the overhead-sun case. The differences between the three ice-crystal results show a significant trend toward lower albedos for larger ice crystals. This trend reflects the values of the asymmetry factors, g, which increase with increasing particle size (Table 1). These results clearly demonstrate that theoretically, at least, cloud albedo is very sensitive to both particle size and shape. Takano and Liou (1989b) performed similar calculations using randomly oriented ice crystals ($L/2a = 125$ μm/50 μm) and area-equivalent ice spheres. The differences in the cloud albedos for the two particles were much like those seen here for the CS and WD models. Thus, it is concluded that simple adjustment of the particle size in the Mie-scattering calculations is insufficient to overcome the differences due to particle shape.

The angular dependence of reflectance is equally important for remote sensing. Variations of this dependence are most easily seen for changes in $\mu_\odot$ and τ_v by normalizing the reflectance by the albedo and displaying the resultant anisotropic factors,

$$\chi_c = \rho_c(\tau_v, \mu_\odot, \mu, \psi)/\alpha_c(\tau_v, \mu_\odot).$$

Figure 6 compares the distributions of χ_c for all four phase functions at $\mu_\odot = 0.8$ and $\tau_v = 1$. The range in χ_c is a measure of the anisotropy in the reflectance field. The three ice crystal reflectance patterns are very similar; however, there is slightly more anisotropy in the CU model than in the CS and C20 results. This difference between the CU and other crystal reflectance patterns persists for all solar zenith angles and optical depths. The WD reflectance distribution is markedly different from those of the three ice crystal types. Significant maxima occur near $\psi = 145°$, $\theta = 45°$ and in the backscattering direction between viewing zenith angles between 60° and 90° for the WD model. The minimum in the side-scattering directions is not evident in the ice-crystal results. The relative maximum in the cirrus phase functions at $\Theta = 156°$ appears in the reflectance patterns in Fig. 6 near $\psi = 125°$, $\theta = 55°$.

Figure 7 shows the variation of the CS and WD anisotropic factors with $\mu_\odot$ for $\tau_v = 4$. The increase in optical depth not only increases the albedo (Fig. 5), it decreases the relative anisotropy. This variation may be seen in a comparison of Figs. 6a and 7a and in Figs. 6c and 7c. The patterns for $\tau_v = 4$ are considerably smoother than those for $\tau_v = 1$, although some of the main features, such as the locations of the relative extrema, are still evident. This trend toward diminished anisotropy gradually continues for increasing optical depths but never results in Lambertian reflectance. Nor does the anisotropy of the CS model converge to that of the WD model at very large optical depths. The

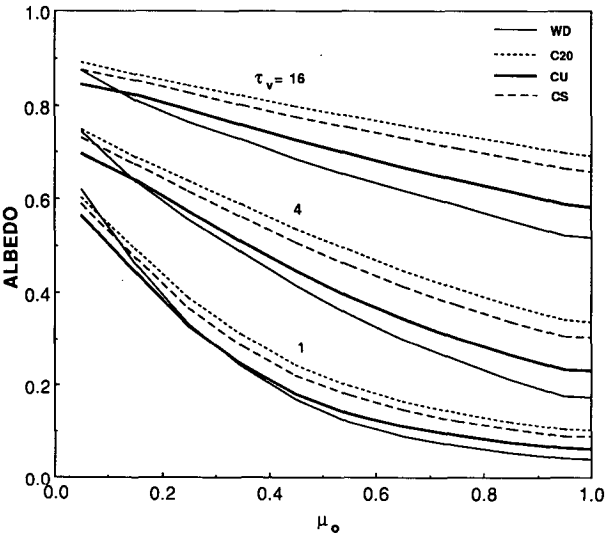

FIG. 5. Theoretical cloud albedos for various phase functions, $\lambda = 0.65$ μm.

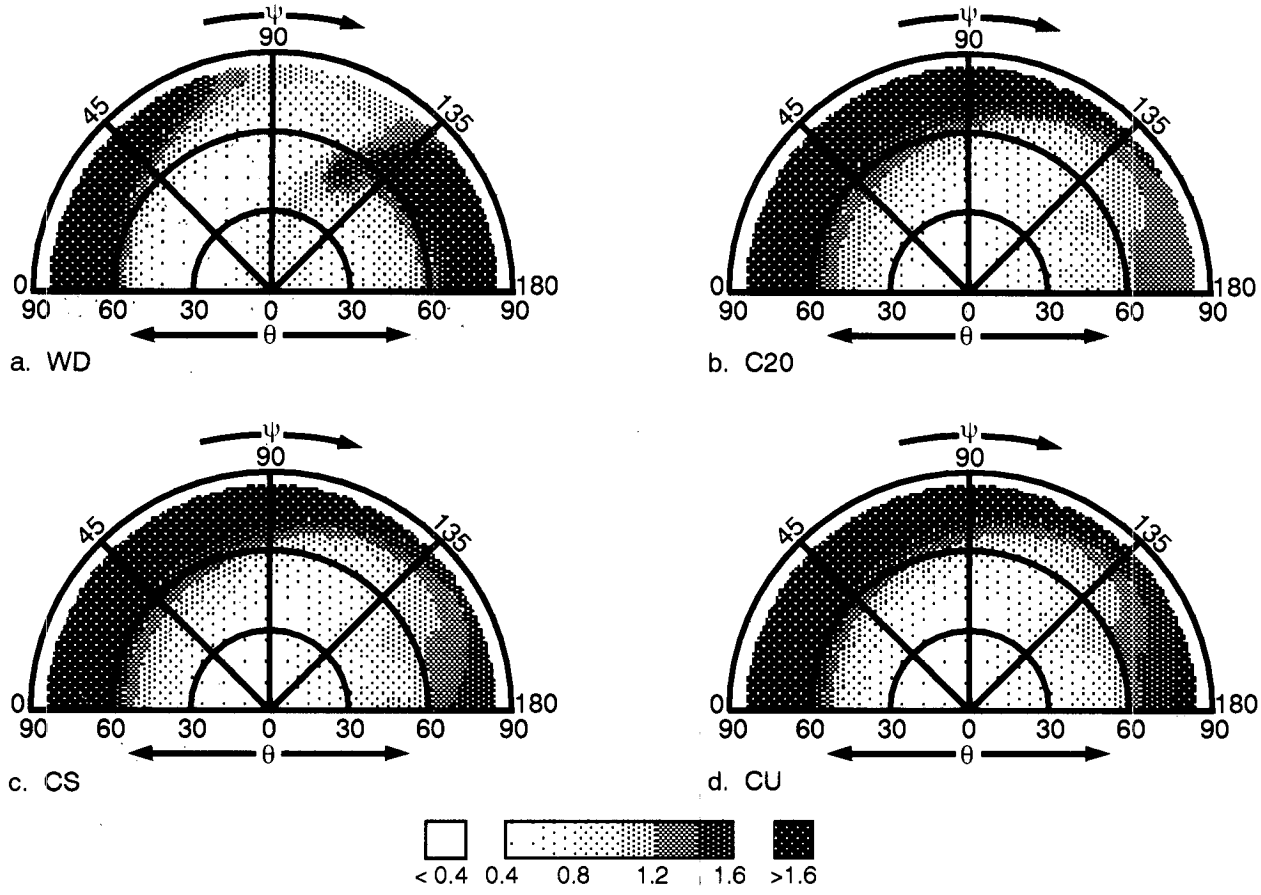

FIG. 6. Anisotropic reflectance factors for $\mu_0 = 0.8$, $\tau_v = 1$, for the WD (a), C20 (b), CS (c), and CU (d) models.

trend of increasing anisotropy with decreasing optical depth continues until the single-scattering limit is reached. Anisotropy also increases with increasing solar zenith angle. Forward scattering becomes more pronounced for both model results. Back reflection increases with θ_0 for the CS model but decreases for the WD case. Minimum reflection occurs along the $\psi \approx 105°$ axis for the WD results. This minimum axis is shifted to $\psi \approx 125°$ for the CS calculations. Despite the relative bias in the albedos for a given optical depth, the differences in the reflectance patterns give rise to certain sets of angles and optical depths for which ρ_c is the same for both the WD and a given ice-crystal model. Such occurrences are most likely whenever a relative minimum from a cirrus model coincides with a relative maximum from the WD result.

c. *Reflectance from combined cloud and Rayleigh layers*

The term, ρ_1, needed to account for the combined reflectance from the cloud and the overlying atmosphere is formulated from theoretical results following the same approach used to account for the contribution of the surface to the measurement in space as given in (14). The beam transmitted to the cloud through the atmosphere having a Rayleigh-scattering optical depth of τ_{R1} and reflected by the cloud back to space may be characterized by some combined transmission and reflection, $T_{R1}\rho_c$, where

$$T_{R1} = \exp[-0.75\tau_{R1}(1/\mu_0 + 1/\mu)],$$

and the empirical factor of 0.75 is used to account for the directionality of the Rayleigh scattering. Its value was estimated by trial and error analysis. The radiation scattered out of the incoming beam is diffuse. The reflectance due to first- and second-order diffuse scattering is approximated as $\alpha_{cd}[1 - \alpha_{R1} - \exp(-0.75\tau_{R1}/\mu_0) + \alpha_{R1d}\alpha_{cd}]$. The Rayleigh albedo is $\alpha_{R1} = \alpha_{R1}(\tau_{R1}, \mu_0)$, and the diffuse Rayleigh albedo is $\alpha_{R1d} = \alpha_{R1d}(\tau_{R1})$. The sum of this term, $T_{R1}\rho_c$, and ρ_{R1} should be approximately equal to the total reflectance at the top of the atmosphere.

Calculations were performed using the adding–doubling model for a pure Rayleigh atmosphere having optical depths corresponding to atmospheric pressures of $p = 250$, 500, 750, and 1000 mb. These results were compiled in lookup tables similar to those developed

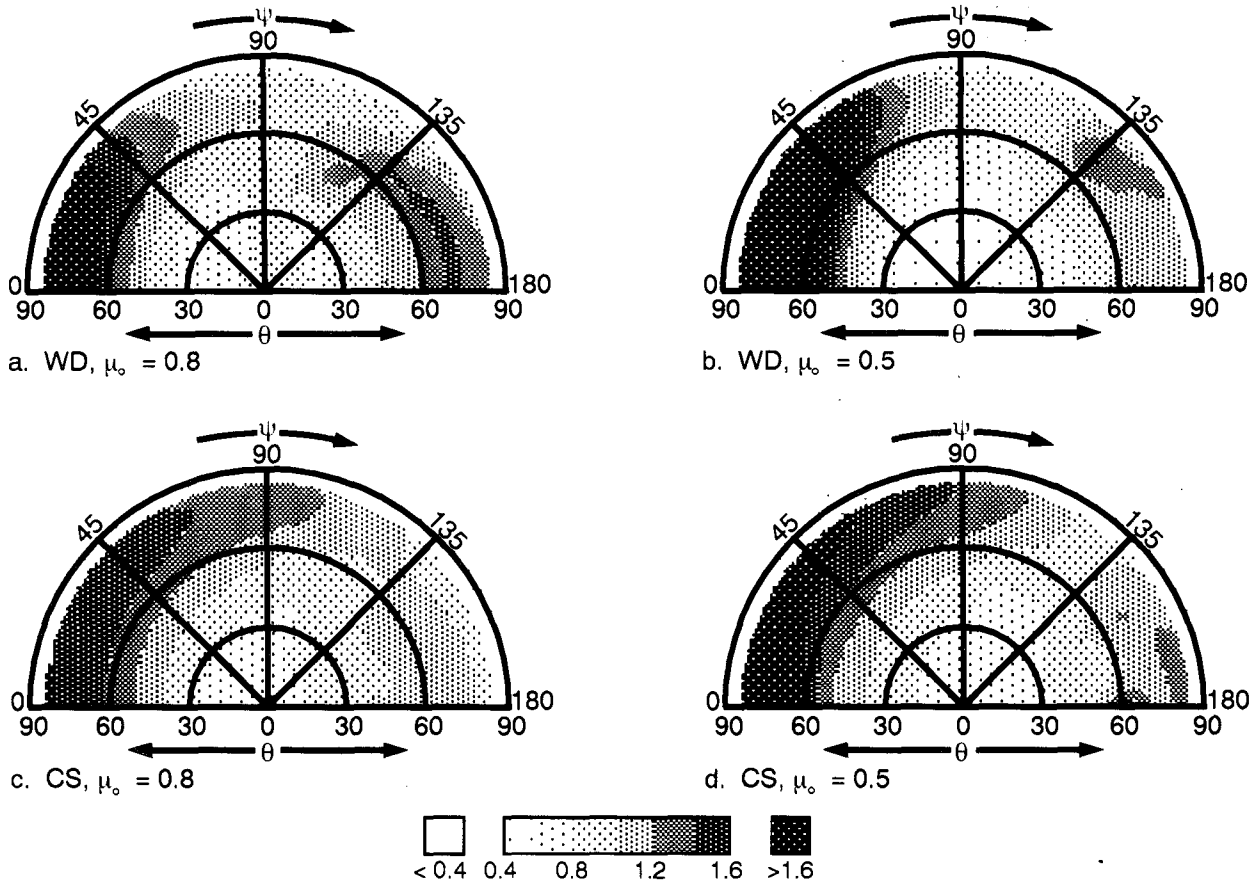

FIG. 7. Examples of anisotropic reflectance factors for $\tau_v = 4$ for WD, $\mu_O = 0.8$ (a); WD, $\mu_O = 0.5$ (b); CS, $\mu_O = 0.8$ (c); and CS, $\mu_O = 0.5$ (d).

for cloud reflectance. Values of α_{R1} and α_{R1d} for a particular set of angles and pressure are determined by linear interpolation between the lookup table values. Calculations were also run for combinations of a Rayleigh layer with a cloud underneath. Cloud optical depths of 0.25, 1, 2, 4, 8, and 16 were used with the C20 phase function. The cloud was placed at $p = 250$ mb and 1000 mb for these computations.

Differences were computed between the results of the radiative transfer model and the parameterization using the lookup tables for Rayleigh reflectance and C20 reflectance for a range of θ_O between 0° and 82°, and for θ between 0° and 70°. It was found that the parameterization tended to underestimate the total reflectance by about 1% at 250 mb and ~2% at 1000 mb. An adjustment factor, $k(p)$, was fitted to these differences using multiple regression analysis. The final form of the model for the combined layers, therefore, is

$$\rho_{c1} = k(p)\{\rho_{R1} + T_{R1}\rho_c + \alpha_{cd}[1.0 - \alpha_{R1} - \exp(-0.75\tau_{R1}/\mu_O) + \alpha_{R1d}\alpha_{cd}]\},$$

where

$$k(p) = 1 + 3.965 \times 10^{-5}p - 1.525 \times 10^{-8}p^2. \quad (15)$$

It was found that the mean error in reflectance for this model is zero, while the rms error varies from 0.90% at 250 mb to 2.43% at 1000 mb. Without the correction for Rayleigh scattering (that is, $\rho_{c1} = \rho_c$), the value of ρ_{c1} would be underestimated by ~5.2 ± 7.5%. This underestimate by the model would translate to an overestimate of ρ_c in the satellite measurement analysis. It is assumed that (15) is valid for any cloud-layer bidirectional reflectance model such as the lookup tables developed for WD, CS, C20, and CU.

A set of lookup tables from adding–doubling results based on combined cloud and Rayleigh layers could be created for each phase function and desired pressure. The model developed here, however, minimizes the amount of computer memory required since only one lookup table is needed to account for Rayleigh scattering for any given atmospheric thickness. The additional available memory permits the inclusion of

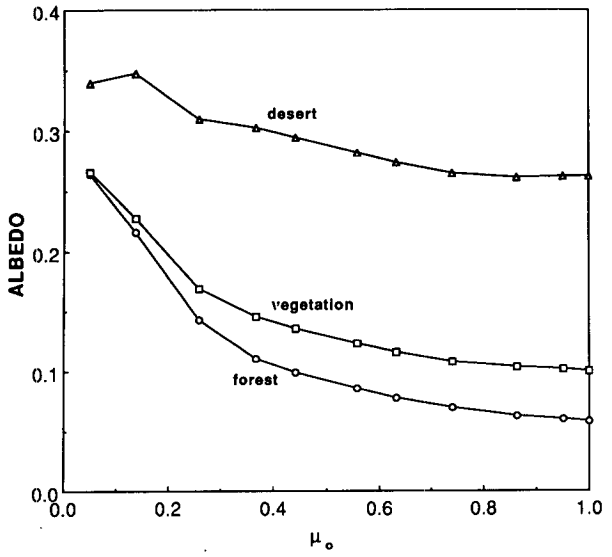

FIG. 8. Clear-sky albedos for parameterization verification.

lookup tables for reflectance patterns from more than one phase function.

d. *Parameterization verification and adjustment*

A similar set of calculations was performed to ensure that (14) provides a realistic representation of the reflectance of the surface–atmosphere–cloud system. The adding–doubling model was run using a Rayleigh atmosphere with ozone absorption over a surface with the reflectance,

$$\rho_g = \rho_g(\mu_o, \mu, \psi)$$

to compute theoretical values for ρ_s and α_{sd}. These computations were performed using several averages of the surface bidirectional reflectance measurements of Kriebel (1978) taken over a coniferous forest and pasture. Reflectances measured at $\lambda = 0.606$ and 0.866 μm were suitably weighted and averaged to simulate reflectances between 0.55 and 0.75 μm. The pasture and forest results were averaged to produce a new model designated as vegetation. To test the parameterization for a realistic range of nonsnow surfaces, the pasture reflectances were doubled. This model is designated as desert. Three surface reflectance models were finally used: coniferous forest, vegetation, and desert. The clear-sky albedos are plotted in Fig. 8. The forest reflectances ($\alpha_{sd} = 0.085$) are similar to water (e.g., Minnis and Harrison 1984); the vegetation albedos ($\alpha_{sd} = 0.122$) are typical of vegetated land (Minnis et al. 1990a); and the doubled pasture reflectances ($\alpha_{sd} = 0.278$) are similar to those of many desert areas (Suttles et al. 1988).

The anisotropic surface reflectance was incorporated into the model by interpolating the measurements to the Gaussian points and representing the azimuthal variation with a Fourier expansion. It was found that 20 Fourier terms were required to reproduce the original data to an accuracy better than 1%. Results were stored for each 15° of relative azimuth angle.

These calculations were repeated with the addition of a cloud layer inserted between the two Rayleigh layers. The surface was placed at 1013 mb, while the top of the lower Rayleigh layer was placed at 900 mb to simulate a low cloud and at 100 mb for an extremely

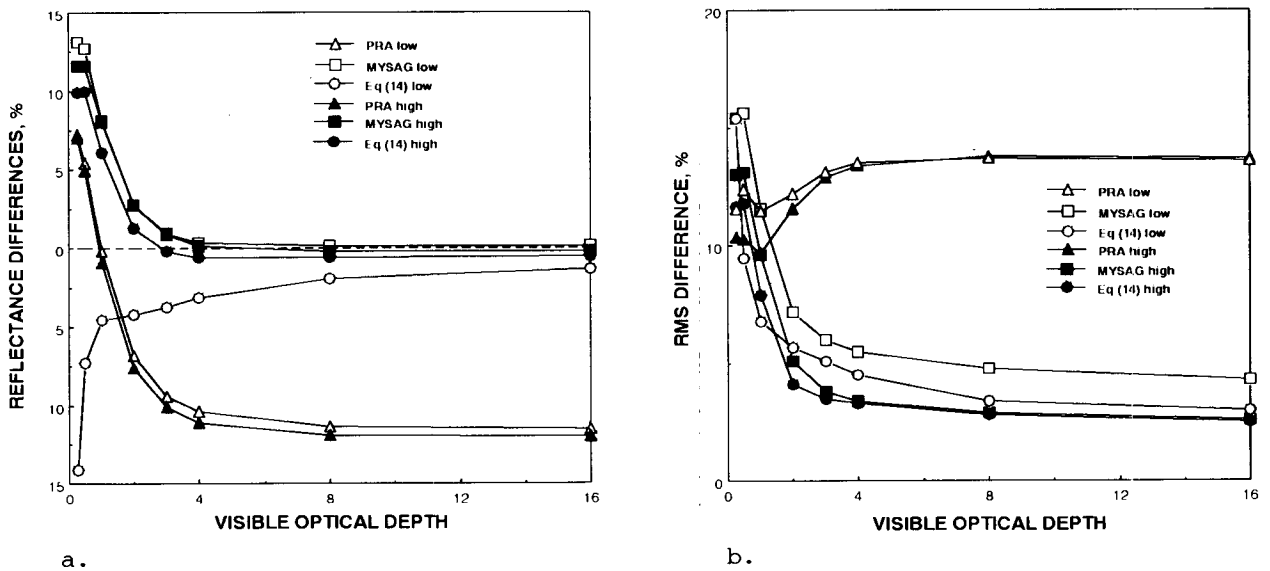

FIG. 9. Reflectance differences between radiative transfer model and parameterizations over forest surface using CS model: (a) mean and (b) rms.

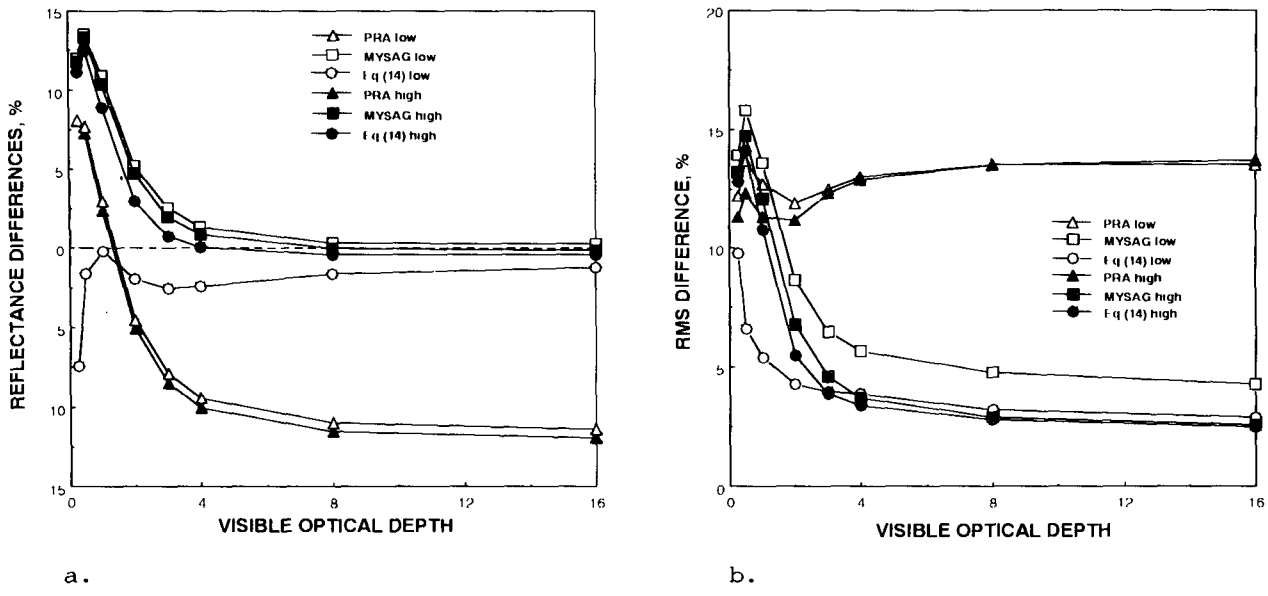

FIG. 10. Reflectance differences between radiative transfer model and parameterizations over vegetated surface using CS model: (a) mean and (b) rms.

high cloud. Cloud optical depths ranged from 0.25 to 16. Sensitivity to cloud type was tested by performing the computations using both the CS and WD models.

Differences between the adding–doubling results and the parameterized total reflectance using (14) were computed at each 15° of ψ for $0° \leq \psi \leq 180°$ for ten selected angles in the intervals $0° \leq \theta_O \leq 82.6°$ and $0° \leq \theta \leq 72.6°$. The results for $\theta = 72.6°$ were not used for $\theta_O = 82.6°$. Numerical problems arise in the radiative transfer models for cloud reflectances at combined high viewing and solar zenith angles. To test the parameterization refinements, the differences were also computed for reflectances calculated with the models of Platt et al. (1980) and Minnis et al. (1990a). The former,

$$\rho = \rho_c + T_c\downarrow T_c\uparrow \rho_s + \alpha_{sd}(1 - \alpha_{cd})(1 - T_c\uparrow - \alpha_c),$$

is designated PRA, while the latter, designated MYSAG, differs from PRA only in the first term, which

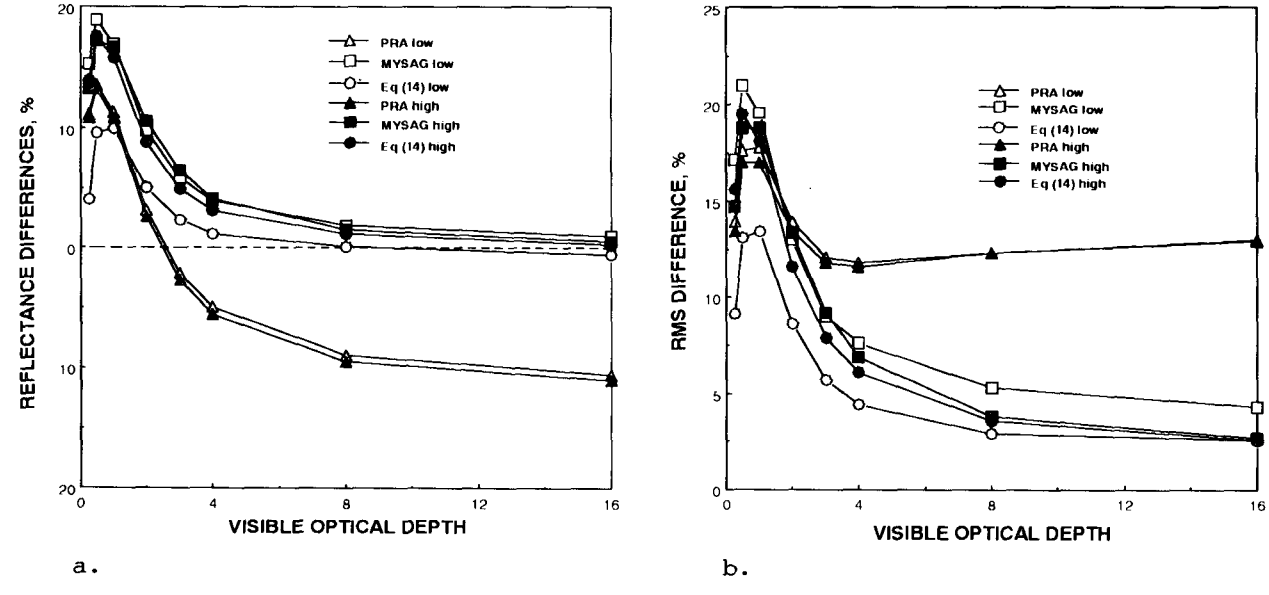

FIG. 11. Reflectance differences between radiative transfer model and parameterizations over desert surface using CS model: (a) mean and (b) rms.

becomes $T_{a1}\rho_c$. In both of the earlier parameterizations, $f_D = 0.5$ in (11) and (12).

Figures 9–11 summarize the results for the three different parameterizations using the CS model applied to the selected backgrounds and cloud heights. Except for a few low-cloud cases, the PRA parameterization produces the smallest mean differences (adding model minus parameterization) for $\tau_v < 4$. At larger optical depths, the PRA rms differences are always greater than the other parameterizations. The PRA model tends toward a constant overestimate of reflectance of ~11% at the larger values of τ_v. In terms of overall mean and rms differences, (14) yields the best agreement with the adding–doubling results. The differences tend to be the least for the darker surfaces (Figs. 9–10) and greatest over desert (Fig. 11). The influence of the Rayleigh scattering is evident in the separation of the mean differences for low and high clouds in the present results. Over darker surfaces at low optical depths, the included Rayleigh scattering is more than expected for low clouds, while it is insufficient for high clouds. The better agreement for the PRA parameterization at small optical depths is probably fortuitous because of compensating effects. The ozone absorption decreases the reflectance while the Rayleigh scattering tends to increase it. At larger cloud optical depths, the Rayleigh scattering becomes relatively less important than the ozone absorption leading to the overestimate of reflectance by the PRA model. This phenomenon helps explain the MYSAG results that yield nearly unbiased results for $\tau_v > 4$ ($\tau_v \gg \tau_{R1}$).

An exact match between the model and parameterization results is not expected because of the complexity of multiple-scattering processes; however, the largest relative errors for the present model occur within the range of optical depths for which accuracy is most important. Very little height correction is needed for clouds with $\tau_v > 4$. Errors as small as 10% in the reflectance can translate into errors as large as 2 km in cloud height for thin clouds. Therefore, a better parameterization is needed to realize any substantial improvement in VIS–IR cloud height retrieval.

Figures 9a–11a indicate that there is a dependence of the parameterization error on cloud height, especially at low optical depths. Multiple-scattering interactions between the Rayleigh layers and the clouds are apparently insufficiently described with (14). A higher-order scattering term was formulated to account for the relative thickness of the two Rayleigh layers. This function,

$$\rho_4 = [\rho_{R2}(1 - \alpha_c^{0.5}) - \alpha_{R1}\alpha_c^2](1 - \alpha_{cd}), \quad (16)$$

is similar to ρ_3 except that its final form was determined from stepwise multiple regression analysis and trial and error. The effects of the two Rayleigh layers are included by using the direct Rayleigh reflectance term for the bottom layer and the Rayleigh albedo for the top layer. Combining (14) and (16) gives

$$\rho = \rho_1 + \rho_2 + \rho_3 + \rho_4. \quad (17)$$

Examples of the results are shown in Fig. 12 for the desert surface. In this case, both the mean and rms errors, especially for the small optical depths, have been reduced relative to errors resulting from using (14). The addition of ρ_4 has eliminated much of the dis-

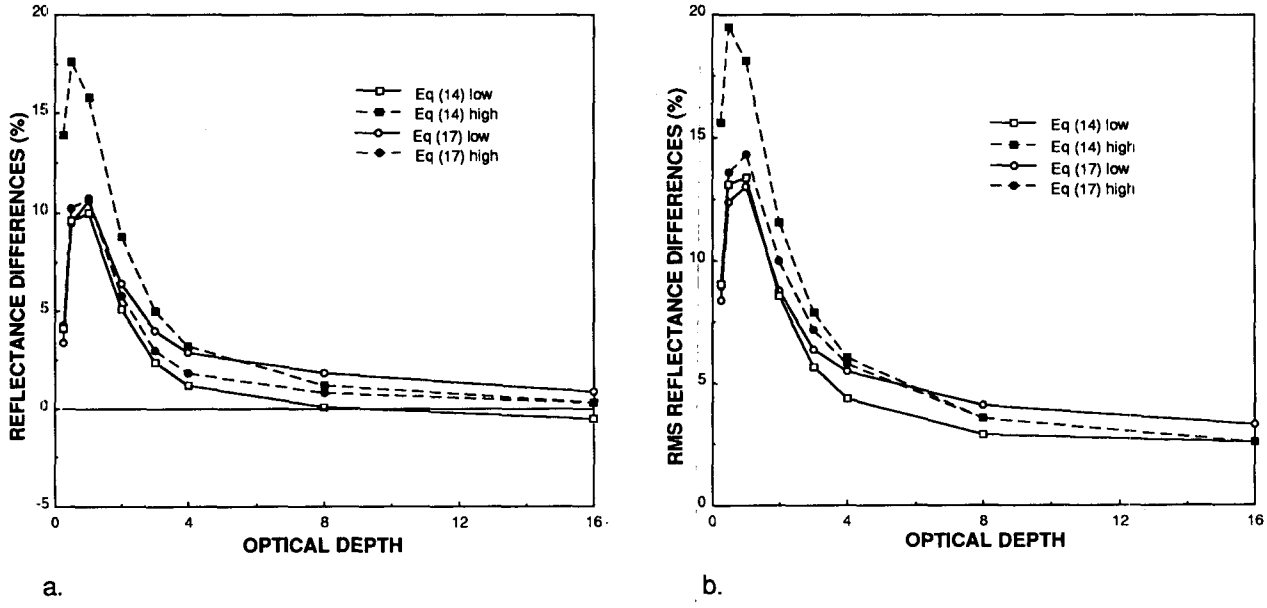

FIG. 12. Reflectance differences between radiative transfer model and two parameterizations over desert surface using CS model: (a) mean and (b) rms.

crepancy in the reflectance errors due to cloud height differences. The results for the other two surfaces are consistent with those in Fig. 12 except that the magnitudes of the changes are smaller.

Despite the improvement gained with the addition of ρ_4, mean and rms errors greater than 10% still remain in the parameterization. Within the low optical depth range (that is, $\tau < 4$), the bias accounts for much of the rms error. The peak in the mean error in Fig. 12, between $0.5 < \tau < 1$, is typical of the results for all cases. This behavior suggests that there is less surface-reflected radiation returning through the cloud than allowed in (17). Additional correction for this phenomenon requires a function of τ and the surface reflectance that peaks at low values of τ and diminishes rapidly with increasing optical depth. Several functions were tested using a least squares regression analysis on the errors from (17). The regression formula producing the lowest errors is

$$\rho_5 = a_0 + a_1\left(\frac{\tau}{1+\tau^2}\right)^2 \mu_0^2 \alpha_s + a_2 \alpha_{sd}, \quad (18)$$

where the regression coefficients, a_i, are listed in Table 2.

Remaining biases from the sum of (17) and (18) were minimized by fitting the mean percentage residuals to

$$\zeta = b_0 + b_1 \ln\tau + b_2 \alpha_{sd} \ln\tau + b_3 \alpha_{sd}, \quad (19)$$

where the variables, b_i, represent the regression coefficients. The values of b_i are listed in Table 3 for all four models. The magnitudes of the coefficients are similar for all of the microphysical models.

The final parameterization for estimating the reflectance for a single-layer cloud embedded in a Rayleigh atmosphere over a reflecting surface is

$$\rho = (\rho_1 + \rho_2 + \rho_3 + \rho_4 + \rho_5)/(1 - \zeta). \quad (20)$$

Errors in the reflectances predicted with this parameterization are plotted in Fig. 13 for the CS model. The mean errors have been reduced to less than ±3.5% for all cases, while the rms errors vary from 2% to 7% depending on the optical depth. The average rms error for the CS model is 5.0%. Average rms errors for all of the models are plotted in Fig. 14. Errors for the WD model are the greatest of the four with the rms errors ranging from 4% to 7% for an average of 6.6%. The reason for the WD parameterization exhibiting the greatest errors is not obvious, although it may be related to the greater anisotropy of the WD phase function in the back-reflecting hemisphere. Overall, the parameterization errors are considerably reduced from those for (14). Unlike (14), (20) does not reduce to the clear-sky case when the cloud optical depth is zero. In this case, (19) cannot be solved; and ρ_4 and ρ_5 do not necessarily reduce to zero in that instance. These artifacts of the model, which may affect the accuracy of optical depths retrieved for very thin clouds, should be taken into account when it is applied.

TABLE 2. Regression coefficients for Eq. (18).

Model	a_0	a_1	a_2
WD	−0.021	0.981	0.095
C20	−0.015	0.855	0.076
CS	−0.015	0.983	0.067
CU	−0.019	0.940	0.084

TABLE 3. Regression coefficients for Eq. (19).

Model	b_0	b_1	b_2	b_3
WD	−0.042	0.034	−0.100	0.148
C20	−0.048	0.030	−0.116	0.193
CS	−0.052	0.032	−0.124	0.211
CU	−0.038	0.026	−0.110	0.163

To ensure that the parameterization operates as precisely at other pressure altitudes, the adding–doubling code was run for the CS model over vegetation for a cloud at 500 mb. The results were compared to those of the parameterization. The mean parameterization bias was zero and the rms errors were lower than those for the regression results.

4. Cloud infrared emittance parameterization

Cloud particles both absorb and emit radiation at thermal wavelengths. Most previous estimates of cloud emittance (e.g., Reynolds and Vonder Haar 1977; Platt 1979) assume scattering to be negligible. Liou (1974), however, demonstrated that the fraction of infrared radiance that is reflected or scattered by the cloud can be significant. This section develops a technique for accounting for scattering in the determination of the cloud emittance.

a. Radiative transfer calculations

For a cloudy scene, the IR radiance observed by the satellite may be approximated as

$$I_{IR} = B(T) = (1 - \epsilon)B(T_s) + \epsilon B(T_c) \quad (21)$$

or

$$\epsilon = [I_{IR} - B(T_s)]/[B(T_c) - B(T_s)],$$

where T is the equivalent blackbody temperature of the observed radiance, T_s is the equivalent blackbody temperature for a clear scene, T_c is the radiating temperature of the cloud, and B is the Planck function evaluated at 11.5 μm. Following Platt and Stephens (1980), the effective cloud emittance is

$$\epsilon = \epsilon_a + \epsilon'_\gamma, \quad (22)$$

where the beam absorption emittance is

$$\epsilon_a = 1 - \exp(-\tau_{IRa}/\mu) \quad (23)$$

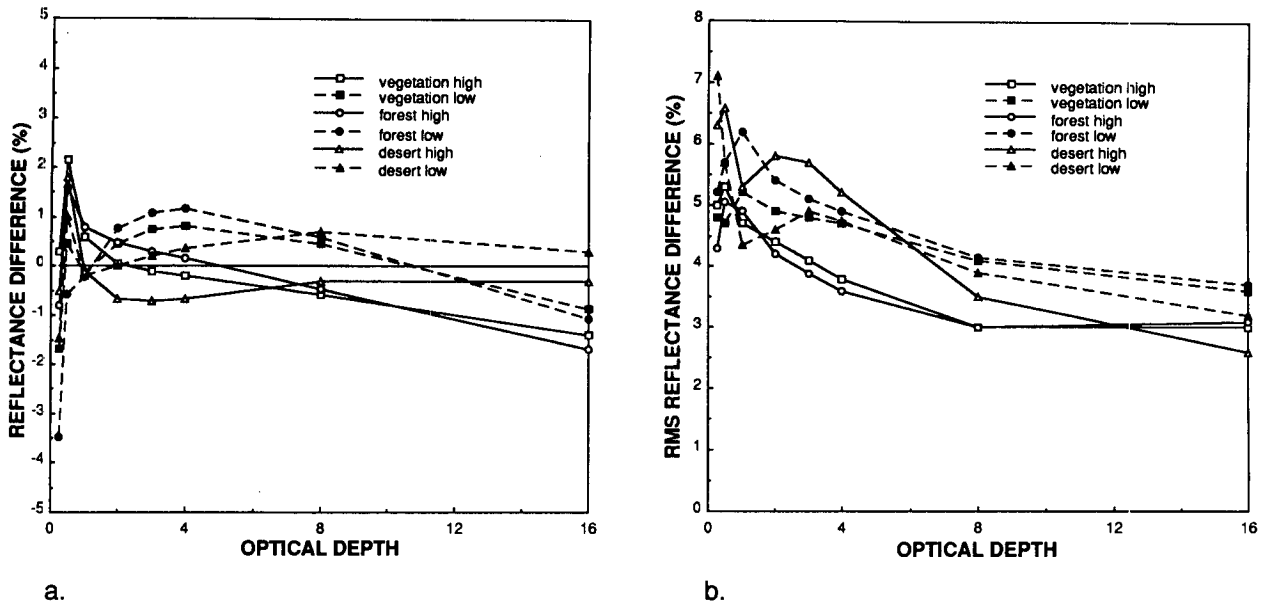

FIG. 13. Reflectance differences between adding–doubling model and final parameterization given by (20) using CS model: (a) mean and (b) rms.

and the effective scattering and reflection emittance is ϵ'_γ. This latter term includes the reflectance of the cloud to the upwelling radiance incident on the cloud base, ρ_{IR}, and the contribution of radiances entering the emergent beam from multiple-scattering processes within the cloud. It is assumed that the water vapor content above the cloud layer is negligible so that there is essentially no downwelling radiance incident at cloud top. The cloud IR absorption optical depth is τ_{IRa}. The contribution of ϵ'_γ to ϵ has been estimated for several sets of conditions by Platt and Stephens (1980) by simulating the cirrus particles as long ice cylinders. A similar approach is taken here to develop a generalized method for estimating ϵ_a from ϵ using more realistic cloud particle shapes.

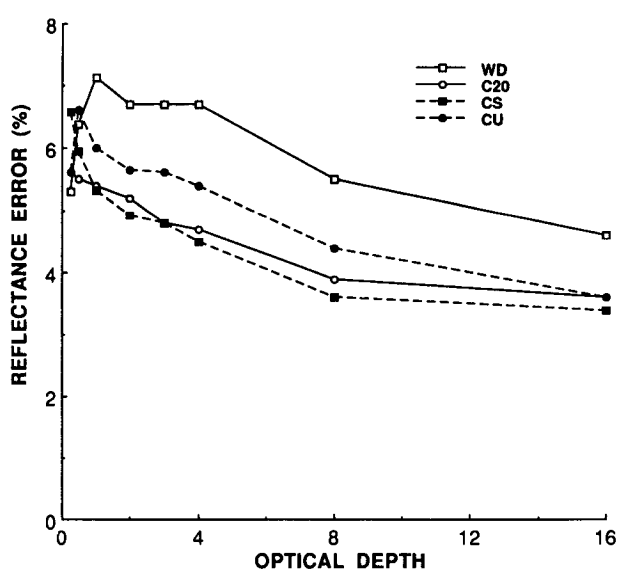

FIG. 14. Average rms errors in reflectance due to VIS parameterization for all surfaces and cloud heights.

Adding–doubling calculations were performed using scattering phase functions for radiation at 10.8 μm for the same particle sizes, shapes, and distributions employed for the VIS reflectance computations. It is assumed that the properties at 10.8 μm are the same as the average properties for 10.5 μm $< \lambda <$ 12.5 μm. Single-scattering albedos at this wavelength are listed in Table 1. The 10.8-μm phase functions for the four particles are shown in Fig. 15. The ice-crystal phase functions were derived using the ray-tracing technique (Takano and Liou 1989a), while the WD phase function was computed using Mie scattering theory. Since azimuthal dependence of the outgoing IR radiances is negligible, no Fourier components were used in the computations. Only the viewing zenith angle dependence is considered here.

The computations were performed for a wide range of surface, cloud, and atmospheric temperatures for a dry atmosphere with relative humidity, RH = 30%, and for a wet atmosphere with RH = 70% to test the sensitivity of effective emittance to these parameters. The top layer of the model was assumed to contain negligible amounts of moisture. Therefore, it contributes essentially nothing to the radiance. An isothermal cloud layer was used with temperatures ranging from 280 K to 210 K in increments of 15 K. The values that were actually used in each case depended on the surface

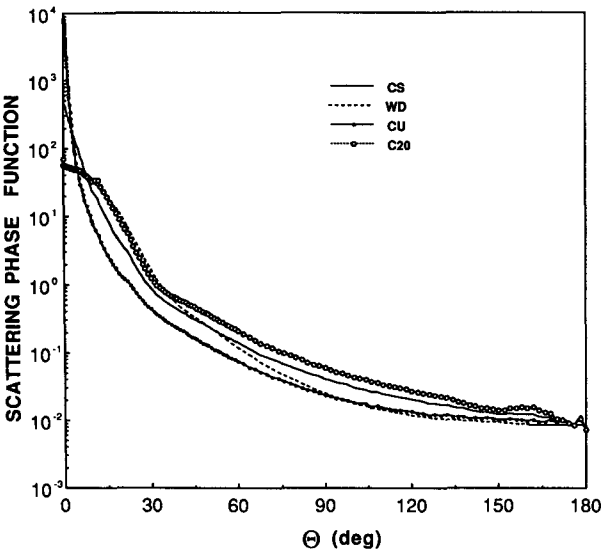

FIG. 15. Scattering phase functions for various cloud particle size distributions, $\lambda = 10.8$ μm.

temperature, T_g, which varied from 320 K to 260 K in increments of 15 K. Temperatures ranged from 280 K to 230 K in the bottom atmospheric layer, the layer containing all of the moisture. In all cases, the bottom-layer temperatures were not allowed to exceed the surface temperature or to be less than the cloud temperature.

The absorption optical depth of the bottom layer was computed using the parameterizations given by Rossow et al. (1988) based on Rothman et al. (1983) for water vapor line absorption,

$$\tau_{wvl} = u_{wv}\frac{0.000067 + 0.0081u_{wv}}{1 + 109u_{wv} + 1.3u_{wv}^{1.6}},$$

and on Roberts et al. (1976) for water-vapor continuum absorption,

$$\tau_{wvc} = 6.386 \times 10^{-6}u_{wv}\{e\exp[1800(1/T - 1/296)] + \delta_p(p - e)\}.$$

The total water-vapor optical depth is

$$\tau_{wv} = \tau_{wvl} + \tau_{wvc}.$$

In these equations, u_{wv} is the layer atmospheric water vapor path (cm-STP), e is the water vapor pressure in millibars, δ_p is 0.001, and the layer temperature T is given in kelvins. Values for τ_{wv} ranged from 0.210 for $T = 280$ K, RH = 70% to 0.001 for $T \leq 250$ K, RH = 30%.

The adding–doubling model was initially run without clouds to obtain $T_s(\mu)$ for each case. Next, clouds with τ ranging from 0.25 to 16 were inserted at the specified temperatures. The effective emittances, $\epsilon(\mu)$, of these clouds were then derived from the results of the clear and cloudy model runs by solving (21). The absorption emittance was also computed from (23) for the same cloud optical depths, where

$$\tau_{IRa} = (1 - \tilde{\omega})\tau_{IR},$$

and τ_{IR} is the cloud IR extinction optical depth.

Figure 16 shows a comparison of the absorption emittance and the effective emittance that includes scattering. These results, computed for a CS cloud with $T_c = 260$ K, $T_g = 290$ K, and RH = 70%, are typical of the effects of scattering on emittance. In general, the effective emittance is 1% to 10% greater than ϵ_a. The largest differences occur for $1 \leq \tau_{IRa} < 4$. At larger optical depths, the absorption increases due to additional multiple scattering so that the relative contribution of pure scattering to the upwelling beam is diminished. The values of ϵ'_γ are reduced at smaller optical depths because the multiple scattering is minimal except at larger viewing zenith angles.

These results are similar to those found by Platt and Stephens (1980) except that the current values of ϵ'_γ are smaller for a given optical depth. The diminished scattering effects are attributable to several factors. Platt and Stephens (1980) used a ten-layer cloud with a base temperature 11 K warmer than its top and defined the absorption emittance relative to the mean cloud temperature. An isothermal cloud was used here. Even without scattering, the absorption emittance of a variable-temperature cloud defined relative to its thermal center will be less than that predicted for one defined by its radiative center. Scattering within an isothermal cloud tends to reduce the emitted contribution from the lower levels that are at the same temperature as the remainder of the cloud. In the Platt and Stephens

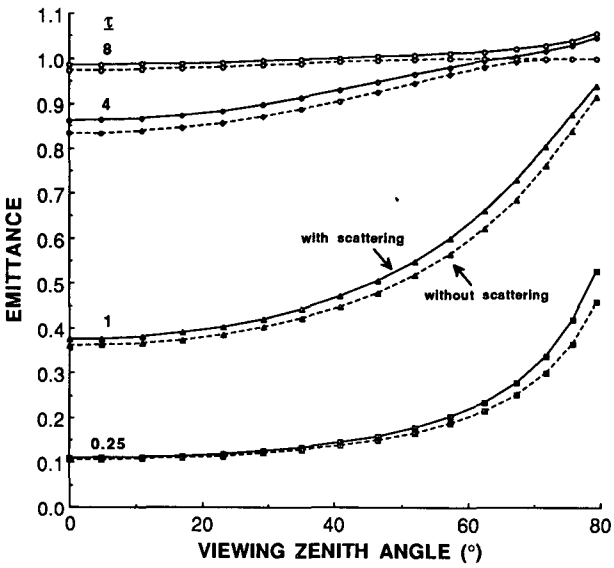

FIG. 16. Effective emittance from adding–doubling calculations using CS model: $T_g = 290$ K, $T_c = 260$ K.

(1980) case, the emission from the lower levels is greater than that from the upper levels, so the reduction in radiance is greater leading to slightly enhanced effective emittance. An isothermal cloud was simulated here because the effective radiating temperature of the cloud is the desired quantity and the primary effect of the scattering is on the upwelling radiation from the surface, not from the cloud. The amount of surface-emitted radiation scattered out of the beam by the cloud depends only on the optical depth of the cloud, its single-scattering albedo, and its scattering phase function. The vertical structure of a given cloud is generally indiscernible from the satellite, so there is little to be gained from a more sophisticated layered-cloud model.

The most important factor driving the effective emittance differences may be the use of ice cylinders by Platt and Stephens (1980). Their ice-cylinder phase functions produce much more back reflectance than the phase functions used here. The former have asymmetry factors ranging from 0.71 to 0.81 compared to $g \approx 0.94$ in Table 1. The range of single-scatter albedos is 0.51 to 0.64 for the ice cylinders and 0.53 to 0.58 for the hexagonal ice crystals. An example of the effect of the variation in the asymmetry parameter on back reflectance is shown in Fig. 5, where the albedo for the C20 model is nearly twice that of the WD model for $\tau_v < 8$. The albedo difference is due only to the change in g from 0.77 to 0.87. The change in g is larger for ice cylinders and crystals at $\lambda = 10.8$ μm. Stephens (1980) calculated the effect of g on the cloud-base reflectance for one set of conditions using $\lambda = 11$ μm and showed a fourfold increase in the amount of back reflectance for a change of g from 0.94 to 0.71. Therefore, it is concluded that the discrepancies between the current effective emittance results and those from Platt and Stephens (1980) are primarily due to the use of different phase functions.

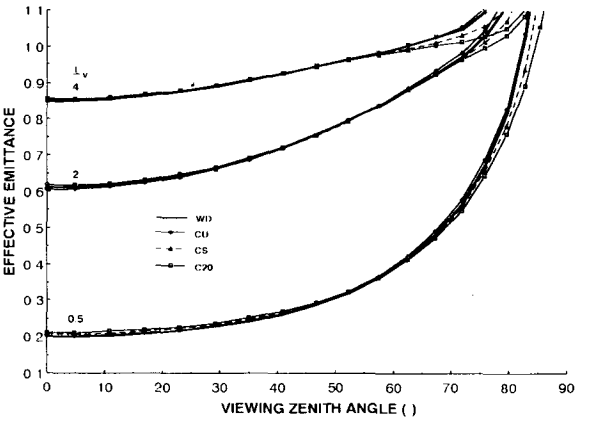

FIG. 17. Effective emittances computed with adding–doubling model for various cloud models using $T_g = 320$ K, $T_c = 270$ K.

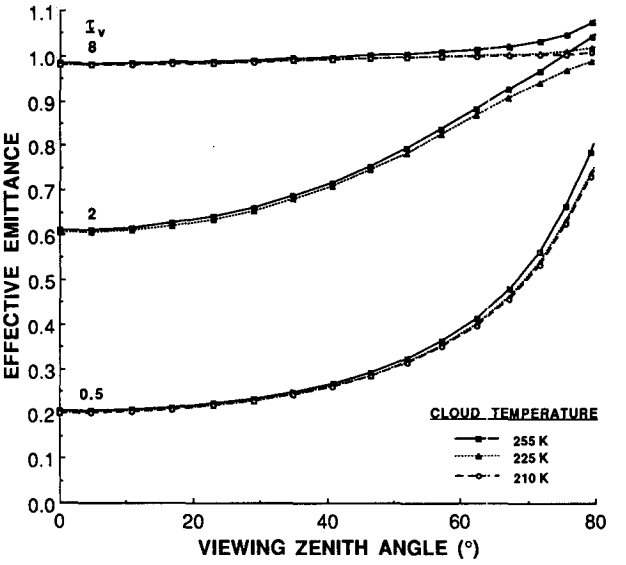

FIG. 18. Variation of effective emittance with cloud temperature for a CS cloud with $T_g = 290$ K.

b. Sensitivity analyses

The influence of cloud microphysics on ϵ is typified in Fig. 17, which shows emittances computed in terms of selected visible optical depths for all four cloud models using $T_g = 320$ K, $T_c = 270$ K, $T_a = 280$ K, and RH = 70%. Values of $\epsilon(\tau)$ are very similar for all four models for $\theta < 70°$. In general, the microphysical variations introduce differences of only 10% or less in the effective emittances. This variation of ϵ may be attributed to a relative balance between the single-scatter albedo and the asymmetry parameter for the ice-crystal models. The C20 emittances are slightly greater than the other ice-crystal results primarily because of substantially weaker forward scattering and a greater value of $\tilde{\omega}$. Since it has the lowest value of $\tilde{\omega}$ and a relatively small value of g, the WD model should produce the greatest emittances. The WD IR extinction efficiency, however, is lower than its VIS counterpart. Thus, the emittance is lower than expected for a given VIS optical depth.

Figure 18 shows the variation of $\epsilon(\tau)$ with cloud temperature for a surface temperature of 290 K using the CS phase function. This result is typical for all surface temperatures. The differences increase with increasing θ but are generally less than 3%. For an average change of 40 K in T_c, the rms change in ϵ is only 2.8% over the range of surface temperatures from 260 K to 320 K and for $\tau \leqslant 8$ and $\theta \leqslant 72°$.

The variation of effective emittance with surface temperature is plotted in Fig. 19 for a CS cloud at 240 K. In this figure, there is little change in the effective emittance for a given optical depth until the cloud temperature approaches that of the surface tempera-

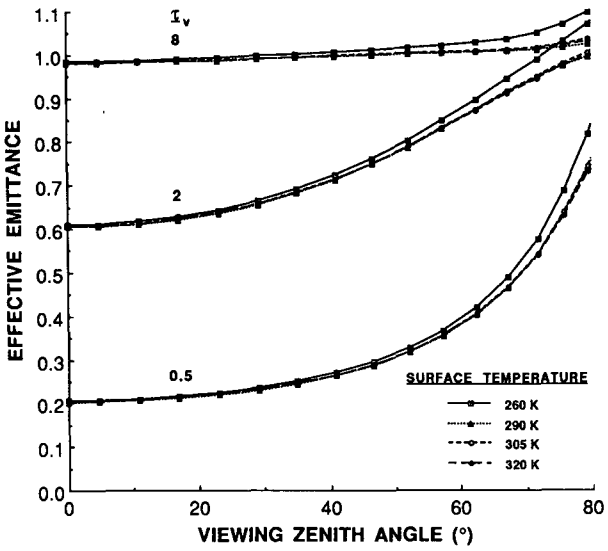

FIG. 19. Variation of effective emittance with surface temperature for a CS cloud at T_c = 240 K.

ture. This apparent increase in emittance with decreased surface–cloud temperature contrast is seen in all of the combinations of surface and cloud temperatures. It arises from the fact that the cloud reflectance has no relationship to the cloud temperature, while the definition of the effective emittance is based on the difference between the cloud and clear-sky temperatures as in (21). To illustrate this effect, consider the simple model adapted from Platt and Stephens (1980),

$$I = I_s(1 - \rho_{IR} - \epsilon_a - \gamma) + \epsilon_a I_c + \gamma f(I_c, I_s),$$

which describes the radiance emerging from the cloud top more accurately than (21). Let the multiple scattering reduce to zero and substitute I into (21). Combining the result with (22) gives the scattering emittance $\epsilon'_\gamma = \rho_{IR} I_s/(I_s - I_c)$. For a given value of ρ_{IR} and I_c, this function increases as I_s approaches I_c. Thus, for this extreme situation, the effective emittance will increase as the surface temperature approaches the cloud temperature. In reality, multiple scattering will tend to dampen the effect. Assuming that the results in Fig. 19 are typical, the rms variation of ϵ is 3.1% for a change in T_g from 320 K to 260 K for $\theta \leqslant 72°$, $\tau_v \leqslant 8$, and T_c = 240 K. The greatest variations occur at large values of θ.

Increasing errors in effective emittance with decreasing cloud–surface thermal contrast do not translate into larger errors in a retrieved cloud temperature. Given a clear-sky temperature, effective emittance, and an observed radiance, (21) can be solved for the cloud temperature or

$$B(T_c) = [I_{IR} - (1 - \epsilon)B(T_s)]/\epsilon. \qquad (24)$$

Figure 20 shows the sensitivity of T_c to errors in ϵ and $T_s - T_c$ for various clear-sky temperatures. For the range of considered ϵ errors, the cloud temperature is accurate to within ±3 K for a contrast of less than 20 K. The errors grow rapidly, however, for greater values of thermal contrast, decreasing surface temperatures, and increasing emittance errors. A smaller rate of increase is apparent for decreasing surface temperature. In summary, this figure shows that the cloud-height retrieval method is most sensitive to errors in effective emittance. Thus, errors in ϵ must be minimized as much as possible.

c. *Parameterization in terms of VIS optical depth*

In previous VIS–IR cloud-height adjustment techniques (e.g., Rossow et al. 1988; Minnis et al. 1990b), the relationship used to determine the cloud emittance from the VIS reflectance is a fixed value for the scattering efficiency ratio, ξ_a. This ratio is

$$\xi_a = \frac{Q_{Vs}}{Q_{IRa}} = \frac{\tau_v}{\tau_{IRa}} = \frac{Q_{Vex}}{Q_{IRex}} \frac{\tilde{\omega}_v}{(1 - \tilde{\omega}_{IR})}, \qquad (25)$$

where Q_{Vs}, Q_{IRa}, Q_{Vex}, and Q_{IRex} are the visible scattering, IR absorption, VIS extinction, and IR extinction efficiencies, respectively. The VIS extinction optical depth is used in this equation since it is equivalent to the scattering optical depth. By deriving τ_v from the VIS radiance measurements and ξ_a from theory, τ_{IRa} can be determined from (25). With no scattering, the effective emittance can be computed using (23), and the true cloud temperature may be found by applying (24) to the measured IR radiance and clear-sky temperature. The values for the extinction efficiencies are the same at both wavelengths for the three ice-crystal

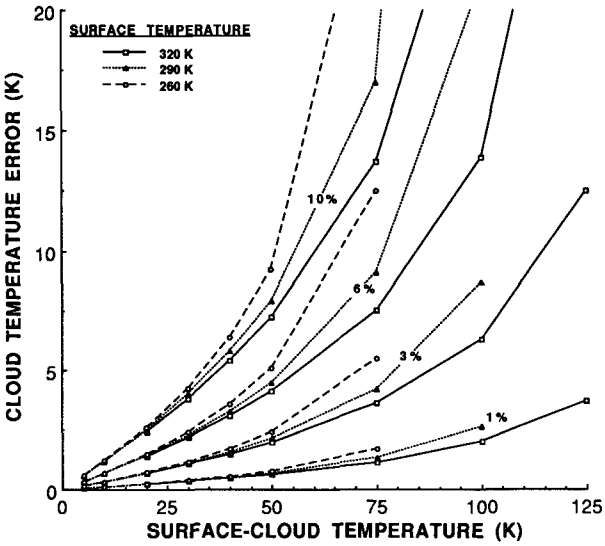

FIG. 20. Sensitivity of retrieved cloud temperature to cloud-surface thermal contrast and errors in effective emittance.

models, while $Q_{V\text{ex}}(\text{WD}) = 2.09$ and $Q_{\text{IRex}}(\text{WD}) = 1.93$ for $\lambda = 10.8$ μm, yielding $\xi_a = 2.30$. At another wavelength typically used for infrared remote sensing, $\lambda = 11.2$ μm, $Q_{\text{IRex}}(\text{WD}) = 1.79$ to give $\xi_a = 2.46$. Thus, there is significant variation in the value of ξ_a within the IR window spectral region for the WD size distribution. The values of ξ_a are 2.14, 2.24, and 2.37 for the CU, CS, and C20 models, respectively.

If scattering effects are important, then an effective scattering ratio,

$$\xi = \frac{\tau_v}{\tau_{\text{IReff}}}, \tag{26}$$

should be used where

$$\tau_{\text{IReff}} = -\mu \ln(1 - \epsilon). \tag{27}$$

The value of τ_{IReff} must be determined empirically from data or theoretical calculations. A mean value of the effective IR optical depth was computed for each microphysical model using the results of the above radiative transfer computations for $\tau_v = 2$, $\theta < 70°$, $T_g = 290$ K, and $T_c = 255$ K, 225 K, and 210 K for the ice-crystal models and $T_c = 270$ K and 255 K for the WD model. These conditions are assumed to represent typical conditions for cirrus clouds and for supercooled water-droplet clouds. The subsequent mean values for ξ are 2.08, 2.06, 2.13, and 2.22 for the WD, CU, CS, and C20 models, respectively. The value of ξ for the CS model is equal to the mean value derived empirically by Minnis et al. (1990b).

Comparing the effective scattering efficiency values to ξ_a shows that neglect of scattering results in errors in the effective IR optical depth ranging from 3.9% for the CU model to 10.6% for the WD model. The effective emittance errors relative to the adding–doubling results were calculated for CS using $\xi = 2.13$ and (23), (26), and (27). Figure 21 plots these errors as functions of viewing zenith angle. There is a significant optical depth effect that causes a range of errors of about 4%. The variation of the errors with θ, however, is as great as 10% for $\theta < 70°$, a typical angular range for cloud or radiative parameter retrieval. Overall, for $\theta < 70°$, the ξ method underestimates the emittance by an average of 0.9% with a standard deviation of 1.5%.

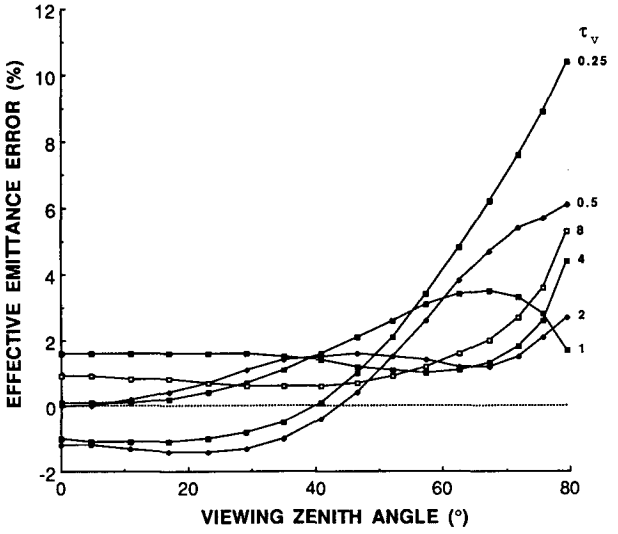

FIG. 21. Effective emittance errors determined from τ_v for CS cloud at $T_c = 245$ K over surface with $T_g = 290$ K using mean scattering efficiency ratio, $\xi = 2.13$.

TABLE 4. Coefficients and errors in Eq. (29) relative to adding–doubling results. Numbers in parentheses refer to averages for $\tau_v < 8$.

Model	a	b	$\overline{\Delta\epsilon_{\text{IR}}}$ (%)	$\Delta\epsilon_{\text{IR}}$ (%)
WD	−0.463	1.041	−0.1 (0.1)	2.2 (2.5)
ID	−0.500	1.000	3.3 (5.0)	5.4 (6.4)
C20	−0.458	1.033	−0.2 (0.0)	2.2 (2.5)
CS	−0.471	1.010	−0.2 (0.1)	1.9 (2.2)
CU	−0.475	1.024	0.0 (0.0)	1.0 (1.0)

Another method for relating the VIS optical depth to ϵ is the parameterization of Liou et al. (1990),

$$\epsilon = 1 - \exp(a\tau_v^b). \tag{28}$$

Equation (28) is essentially the same as the previous method (that is, $a = 1/\xi$) except that the variation of ξ with optical depth is taken into account with the exponent. The errors for (28) were also computed for the same conditions used above employing the coefficient values given by Liou et al. (1990), $a = -0.468$ and $b = 0.988$. The results are nearly identical to those in Fig. 21 with a mean error of 0.9% and a standard deviation of 1.9%.

While this level of error is tolerable, it is desirable to eliminate any bias errors. Thus, the radiative transfer results covering the full range of temperatures for each microphysical model were used in a least squares linear regression analysis using a variant of (28),

$$\epsilon = 1 - \exp[a(\tau_v/\mu)^b], \tag{29}$$

to determine the best set of coefficients for each cloud type. Only the results for $\tau_v < 8$, $\theta < 70°$ were used since the greatest degree of accuracy is needed for the thinner clouds. The resulting coefficients are given in Table 4. The mean and rms errors, $\Delta\overline{\epsilon_{\text{IR}}}$ and $\Delta\epsilon_{\text{IR}}$, respectively, were calculated using all of the adding–doubling results, that is, $\tau_v = 0.25, 16$; $\theta < 70°$. Negative error values indicate that the parameterization overestimates emittance. Correlation coefficients for the first four models are greater than 0.998. The fifth model, denoted as ID in Table 4, refers to the ISCCP droplet model. It is exactly the same as the WD model in the VIS spectrum. The ID model coefficients for (29) are, however, equivalent to the ratio method where $\xi = 2$

and are based on empirical results for ice clouds (see Rossow et al. 1988). Both the WD and ID models are used here because the former represents a theoretical water cloud and the latter is the model actually used by the ISCCP. It is introduced here because it will be evaluated in Part II of this paper.

Although the mean emittance errors are insignificant, they depend on θ in a manner similar to that seen in Fig. 21. Thus, there are some minor bias effects that depend on the viewing angle. The greatest errors in Fig. 21 are found for the smallest optical depths at $\theta > 58°$. Other retrieved cloud parameters (e.g., cloud amount) are subject to increased uncertainty at relatively high viewing angles (Minnis 1989). The viewing angle biases and residual optical depth dependencies give rise to the rms errors in Table 4. Another aspect of using (29) instead of an exact model is that the effective emittances greater than unity cannot be reproduced. Thus, emittances and, therefore, the temperatures of thick clouds will be slightly underestimated. The magnitude of the underestimates will not exceed 1 or 2 K in most cases.

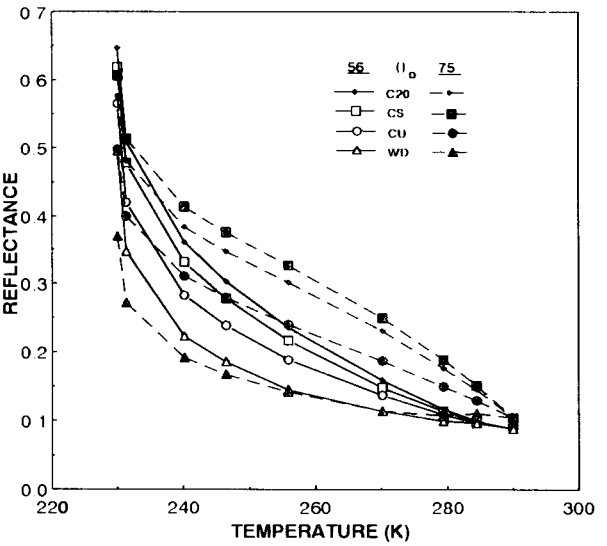

FIG. 22. Effect of microphysics on relationship between observed temperature and reflectance over vegetation.

5. VIS–IR parameterization summary

Parameterizations have been developed separately for VIS reflectance and IR emittance in the previous sections. This section examines the combined models used as an analysis system. Hereafter, the unsubscripted variable τ will refer only to VIS optical depth, since IR optical depth is only used implicitly in the parameterization.

a. Model application

The combined VIS–IR parameterization may be used to simulate the reflectance and equivalent blackbody temperature pair that would be observed by a satellite at any given angle. The required input to this model consists of the Rayleigh reflectance versus pressure lookup tables, a microphysical model lookup table of τ versus ρ_c, α_c, and α_{cd} (e.g., the CS model), a clear-sky anisotropic factor model χ_s, and values for u, T_s, T_c, ρ_s, and α_{sd}. These quantities are used in (20), (29), and (21) and their supporting equations to simulate an observation of a cloud at the height corresponding to the specified temperature, T_c. Values of ρ and T are calculated at each of the values of τ in the lookup tables. Linear interpolation is used to obtain a value of ρ at the specified optical depth. The inverse process is used to derive the values of τ and T_c from a measurement of ρ and T. Linear interpolation between the table values of ρ are used to find τ.

Figure 22 shows a simulation of the reflectance and equivalent blackbody temperatures expected for a cloud having $T_c = 230$ K over a vegetated surface viewed at $\theta = 60°$, $\psi = 165°$ for two different solar zenith angles. The variation of the curves with microphysics is similar to that for albedo (Fig. 5). For a given temperature (emittance or optical depth), the WD model yields lower reflectances than the ice-crystal models. At $\theta_o = 56°$, the C20 reflectance is 70% greater than the WD value over a large range of temperatures. There is little difference between the reflectances for $T > 270$ K. This is not the case for $\theta_o = 75°$, where the WD model is easily differentiated from the other models at very low optical depths. The C20 reflectances are up to 230% greater than the WD values at this particular set of angles. Even the shapes of the curves are different. The differences between the various crystal models are also significant.

An example of the variation of the reflectance–temperature relationship with surface albedo and solar zenith angle is given in Fig. 23 for the CS model, where $\theta = 53°$ and $\psi = 165°$. Except for $\theta_o = 75°$, the thin cirrus clouds add little to the reflectance at these angles. In some cases, the presence of cirrus does not increase the reflectance at all (e.g., $\theta_o = 56°$ over vegetation) or it actually decreases the reflectance (desert, $\theta_o = 30°$ and 56°). Such "invisible" cirrus clouds have been observed in two-dimensional histograms of satellite VIS and IR radiance pairs (e.g., Minnis and Wielicki 1988) and in dual-satellite imagery (e.g., Wylie and Menzel 1989). This reflectance behavior may help explain the occurrence of "dark" pixels noted by Minnis et al. (1990b). In addition to making the cirrus undetectable in the VIS reflectance, the relationship between τ and ρ can be nonmonotonic, producing a nonunique solution for the cloud retrieval. Thus, the method should be applied very carefully, especially over bright surfaces, with cognizance of this behavior.

Figure 24 depicts the theoretical variation of ρ with

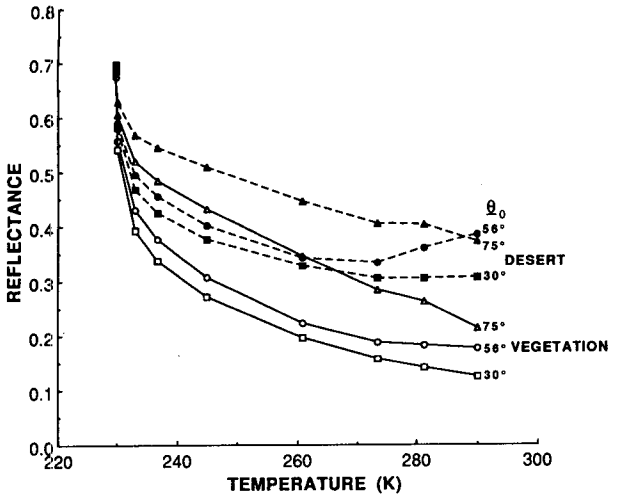

FIG. 23. Dependence of reflectance–temperature relationship on surface albedo and solar zenith angle, $\theta = 53°$, $\psi = 165°$.

T for a WD and a CS cloud located at three different altitudes over a 290 K surface. The angles are $\theta_0 = 56°$, $\theta = 53°$, and $\psi = 90°$. This figure clearly shows the impact of using one model in place of another in a cloud retrieval. For example, at $T = 278$ K and $\rho = 0.13$, the WD model places the cloud at 270 K, while the CS model puts it between 210 and 240 K. Similarly, at $T = 245$ K and $\rho = 0.29$, the CS model would give a cloud at 210 K, while the WD model would yield 240 K, an altitude difference of ~4.6 km. Thus, from a theoretical standpoint, the use of a WD or ID model to interpret VIS and IR radiances from a CS cloud will seriously underestimate the altitude of the cloud in this case if the cloud is optically thin. Conversely, the use of a CS model to interpret a WD cloud would yield an overestimate of the cloud's height. The overlap in the models at certain temperature–reflectance pairs constitutes an ambiguity in the process of retrieving cloud temperatures with this approach. Other clues in the data will need to be used to make the proper model selection in such ambiguous cases.

The cloud temperature differences, ΔT_c, in the ID and CS models were computed for the full range of angles ($\psi = 0$, 180°; $\theta_0 = 0$, 82°; $\theta = 0$, 75°) and temperatures over all three simulated surfaces to obtain a better quantification of this under- or overestimation. All computations were performed using $T_s = 290$ K, $T_c = 270$, 240, and 210 K, and a lapse rate of 6.5 K km^{-1}. The resulting mean biases are plotted in Fig. 25 for the vegetation and desert backgrounds. These bias errors were computed relative to the CS parameterization so they represent an addition to the parameterization error (discussed in the next section). For thin, low clouds, the mean bias is less than 3 K, equivalent to an altitude difference smaller than 0.5 km. As the cloud height increases, the errors become very significant, even for $\tau = 4$. The decreases in ΔT_c for $\tau < 1$ with $T_c = 210$ K over the desert reflects the absence of cases for which no solution could be computed due to extremely low emittances. At large optical depths, it does not matter which model is used to estimate T_c. Assuming that a 240 K cloud is typical, it is expected that, on average, the ID model will underestimate cirrostratus cloud heights by 1 to 2 km for $\tau < 4$. Greater underestimates should be realized at low viewing zenith angles and smaller errors are likely for $\theta > 55°$.

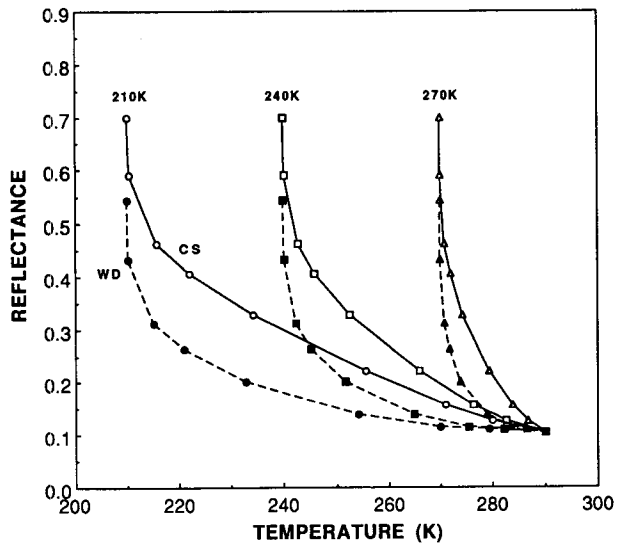

FIG. 24. Reflectance–temperature curves for CS and WD models at $\theta_0 = 56°$, $\theta = 53°$, $\psi = 90°$.

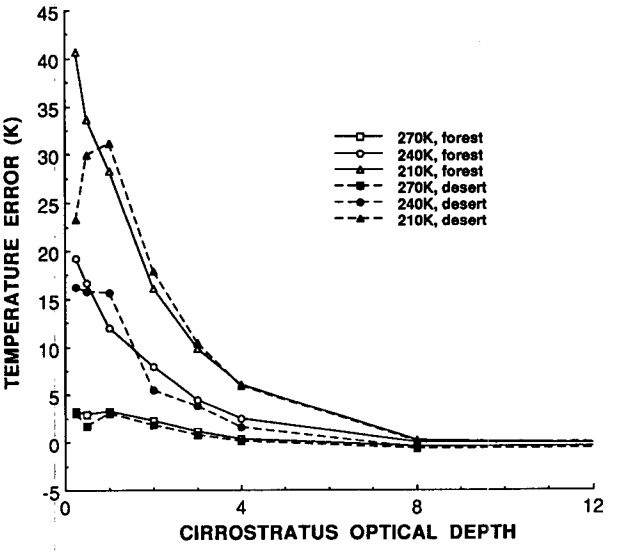

FIG. 25. Bias errors in retrieved cloud temperature using ID model to interpret cirrostratus reflectance.

b. Total parameterization errors

In the cloud parameter retrieval system, the optical depth is the means to obtain emittance and, subsequently, cloud temperature. Rms errors in the effective emittance, $\Delta\epsilon_v$, due to uncertainties in τ are found by introducing optical depth errors into (29). The optical depth errors were estimated by applying the retrieval method described in the previous section to the reflectances computed with the adding–doubling routine. The resulting optical depth errors were computed by differencing the τ values used in the radiative transfer model and those found using the retrieval method. The results are summarized in Fig. 26 for the CS parameterization. Over the darker surfaces, the optical depth errors vary from 12% to 33%. Extremely large errors, up to 135%, are obtained over the bright desert surface. The increase of error with surface albedo demonstrates the small effect of the cloud's presence on the total reflectance when it overlies a bright surface. Discrimination of a cloud from the background is much more difficult over a bright surface. More reflective surfaces such as snow or an underlying cloud would be expected to produce even larger errors.

The maximum errors, incurred for $2 \leqslant \tau \leqslant 4$, are primarily the result of reflectance in the forward-scattering (that is, $\psi \leqslant 15°$, $\theta_0 > 60°$, $\theta > 60°$) and backscattering ($\Theta \approx 180°$) directions where small increases in optical depth produce substantial changes in the reflectance. If the forward and backscattering angles are removed from the error analysis, the optical depth errors reduce to less than 10% for all optical depths over vegetation.

The effective emittances were calculated using the optical depth errors to obtain $\Delta\epsilon_v$. The results are plotted in Fig. 27 for desert and vegetation. The forest results are nearly identical to the latter. These errors are not as great as those found in Fig. 26. At low values of τ, the optical depth error is almost linear with emittance error. As the emittance approaches unity, the optical-depth error becomes less significant as expected.

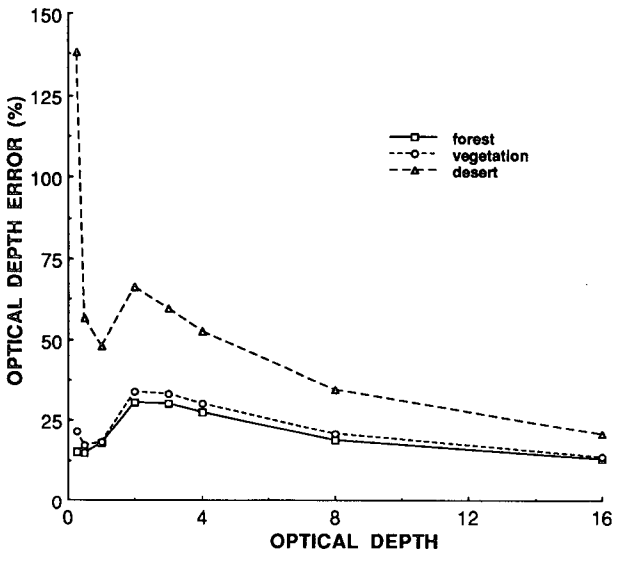

FIG. 26. VIS parameterization optical depth errors.

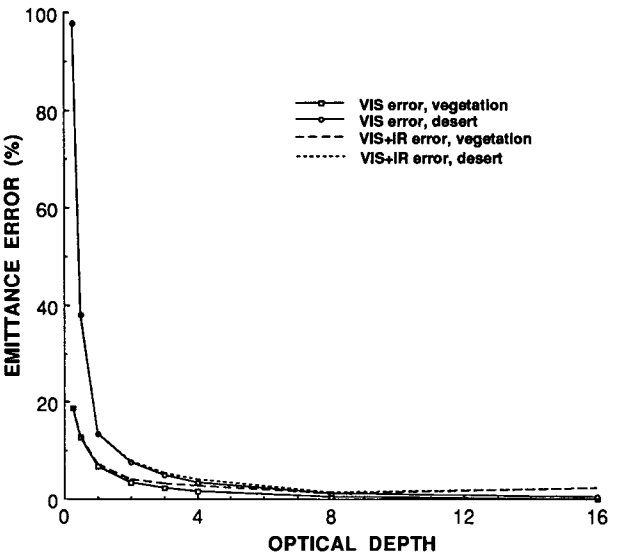

FIG. 27. Emittance errors due to VIS and IR parameterization errors.

Assuming that the IR and VIS errors are statistically independent, the total rms effective emittance error in the combined retrieval system is

$$\Delta\epsilon = (\Delta\epsilon_{IR}^2 + \Delta\epsilon_v^2)^{1/2}. \qquad (30)$$

The overall errors computed with (30) are also summarized in Fig. 27 for the CS model. The IR error is insignificant for thin clouds. Since $\Delta\epsilon_v \to 0$ for thick clouds, the IR error dominates for $\tau > 4$. The increase in the rms error for $\tau = 16$ reflects the lack of emittances greater than unity in the parameterization as noted earlier.

The overall errors in ϵ are converted into errors in retrieved cloud temperature in Fig. 28. Errors for the vegetation are nearly the same as those for the forest case. The mean error, an overestimate of the cloud temperature at low optical depths, results from the nonlinearity of the Planck function and the inability to retrieve a temperature in certain conditions. A significant portion of the rms error is due to this bias effect for $\tau < 1$. As discussed in Minnis et al. (1993), however, this bias may not be realized in application of the parameterization. From Fig. 28b, it appears that a typical cloud temperature (e.g., $T_c = 240$ K) or cloud height may only be determined to within ±12 K or ~ ±2 km, respectively, over an average background if the cloud is very thin ($\tau \leqslant 0.25$). Thicker cloud heights

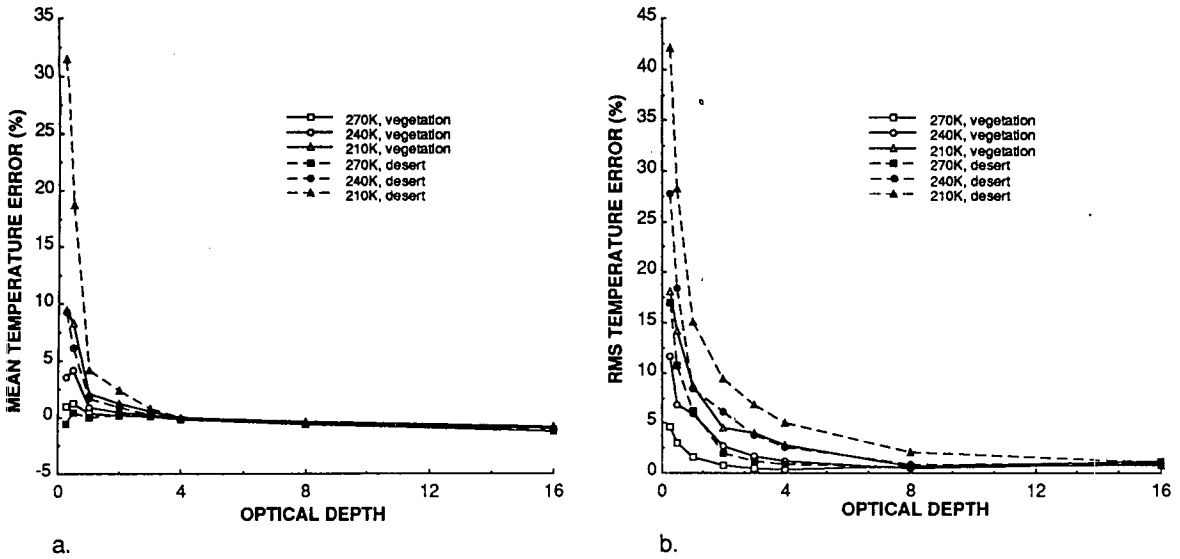

FIG. 28. Retrieved cloud temperature errors due to total parameterization errors: (a) mean and (b) rms.

may be determined more accurately. Over deserts, the cloud temperatures are much more uncertain.

As shown in sections 3 and 4, the combined VIS–IR parameterization reproduces the reflectance and radiant temperature field with good precision relative to the adding–doubling model. Small errors in reflectance (<5%), though, produce significant errors in optical depth and emittance for thin clouds. This large uncertainty suggests that "exact," that is, adding–doubling, calculations should be used for the thin cloud conditions. Such exact calculations, however, are not warranted because of the extreme sensitivity of τ to errors in ρ in the case of thin clouds. For example, the 5% error in reflectance is, conservatively, the accuracy of the clear-sky reflectance. The difference between hazy and high-visibility conditions is due to a change in aerosol optical depth, say, of ~0.4. Such variations are not usually taken into account with most satellite retrieval methods. Thus, even with "exact" modeling, the cloud temperature retrieval errors in Fig. 28 are as likely to occur in practice as they would if the parameterization was used.

6. Summary and conclusions

This study has demonstrated the need for examining the VIS–IR bispectral technique for inferring cloud height and optical depth and, specifically, the technique used by the ISCCP as applied to cirrus clouds. The ISCCP technique uses a radiative transfer model based on scattering by water droplets to infer the optical depth of all clouds observed by the VIS channel of the satellite. The ISCCP methodology was developed before realistic ice-crystal scattering phase functions were developed. Several ice-crystal phase functions have since become available. This study analyzed, from a theoretical viewpoint, the impact of using various phase functions to interpret the radiances from cirrus clouds observed by satellites.

A parameterization of reflectance and emittance in terms of various cloud microphysics was developed from adding–doubling radiative transfer calculations to examine the VIS–IR technique for cloud analysis. The parameterization of reflectance at visible wavelengths accounts for ozone absorption, Rayleigh scattering, and anisotropic surface reflectance. It requires lookup tables of cloud reflectance as a function of optical depth and the viewing and illumination conditions. Accommodation of the parameterization to various cloud microphysics requires the determination of several coefficients using the results of some adding–doubling calculations in a simple regression analysis. Coefficients were derived for four different microphysical models. It was found that the parameterization can reproduce the top-of-the-atmosphere reflectance from clouds to within ±6% over surfaces having albedos between 0.08 and 0.28. This parameterization reduces the reflectance uncertainties for thin clouds by a factor of 2 from previous parameterizations. It also eliminates the bias errors associated with the earlier approximations.

The IR parameterization was developed from the adding–doubling calculations in terms of effective emittance. Scattering effects can alter the cloud emittance by as much as 10%. It was found that the theoretical effective scattering efficiency ratio derived from the adding–doubling calculations for the CS model, 2.13, is the same as that derived empirically from a combined lidar–satellite data analysis (MYSAG). This value is 5% lower than expected for a nonscattering

cloud. Therefore, methods that neglect scattering in the IR spectral region will tend to underestimate the effective emittance. The parameterization was developed for the same four microphysical models used in the VIS modeling. Its application requires only a pair of regression coefficients, the VIS optical depth, and the viewing angle to determine the effective emittance. The effective theoretical emittances for cloudy conditions can be simulated with the model to a precision of 2% for viewing zenith angles between 0° and 70°.

The combined parameterizations were used to simulate retrievals of cloud optical depth and cloud temperature for thin clouds. It was found that typical optical depth errors due to the parameterization are on the order of 25% over a dark surface and much greater for brighter surfaces. These errors translate to uncertainties in the derived cloud heights as great as 3 km for very thin ($\tau \sim 0.25$), high clouds over average surfaces and up to 7 km for the same clouds over desert surfaces. The errors are considerably smaller for less extreme conditions. While such large relative errors impact height assignment and the microphysical quantification of the clouds, they have a much smaller effect on the radiation fields estimated for the retrieved clouds. The parameterization's radiance errors, as noted above, are four times smaller than the optical depth errors. Despite the large uncertainties in the parameterization retrievals for very thin clouds, it was concluded that the errors over the darker surfaces are acceptable given the sensitivity of the retrievals to other error sources. These other errors, which are encountered in actual retrievals, are the same magnitude or greater than the parameterization errors.

Calculations performed with the parameterizations were used to demonstrate variations of the reflectance and temperature fields with changes in the background, angular conditions, and microphysical model. Significant differences were found in the reflectance–temperature relationships as a result of using different microphysical models to simulate the clouds. Although the models can produce nearly the same results at a few particular angles, the smaller-particle ice crystal models (CS and C20) produced quite distinct results, on average, compared with the water droplet model used by the ISCCP. There are innumerable microphysical configurations for cirrus ice crystals (plates, oriented columns, bullet rosettes, aggregates, etc.) that were not considered here. The other configurations may produce somewhat different results and should be examined in the future.

This study has highlighted several problems with cloud temperature retrievals using a VIS–IR technique. The reliability of a given retrieval decreases dramatically as the background albedo increases. Therefore, this method may not be particularly suitable to application over bright deserts or snow. Very high, thin clouds are also difficult to discern, even over dark backgrounds. Small emittance errors can lead to large temperature errors in these conditions. It is also evident that there are many conditions that arise that are microphysically ambiguous. The single microphysical model used by ISCCP requires no distinction between water and ice clouds. Having water droplet and ice crystal models, however, generates the practical problem of determining whether the observed cloud is ice, water, or both. Despite such potential difficulties, it appears that there are significant microphysical differences in cloud reflectance that should be taken into account. As in any theoretical study, however, the overall utility of a given technique is not known with confidence until it is applied to observations. Part II of this paper (Minnis et al. 1993) takes that next step to determine if the theoretical microphysical models used in this study are applicable to the real world of cloud property retrieval from satellites.

Acknowledgments. This work represents part of the Ph.D. dissertation of Patrick Minnis. The assistance of D. F. Young of the Lockheed Sciences and Engineering Company in the development of the graphics is gratefully acknowledged. The research efforts of K.-N. Liou and Y. Takano have been supported by NASA Grant NAG1-104A.

REFERENCES

Arking, A., 1964: Latitudinal distribution of cloud cover from Tiros III photographs. *Science,* **143,** 569–572.

——, and J. D. Childs, 1985: Retrieval of cloud cover parameters from multispectral satellite images. *J. Climate Appl. Meteor.,* **24,** 322–333.

Chahine, M. T., 1974: Remote sounding of cloudy atmospheres. I. The single cloud layer. *J. Atmos. Sci.,* **31,** 233–243.

Coakley, J. A., Jr., and F. P. Bretherton, 1982: Cloud cover from high-resolution scanner data: Detecting and allowing for partially filled fields of view. *J. Geophys. Res.,* **87,** 4917–4932.

Heymsfield, A. J., and C. M. R. Platt, 1984: A parameterization of the particle size spectrum of ice clouds in terms of the ambient temperature and the ice water content. *J. Atmos. Sci.,* **41,** 846–855.

Inn, E. C-Y., and Y. Tanaka, 1953: Absorption coefficient of ozone in the ultraviolet and visible regions. *J. Opt. Soc. Amer.,* **43,** 870–873.

Kriebel, K. T., 1978: Measured spectral bidirectional reflectance properties of vegetated surfaces. *Appl. Opt.,* **17,** 253–259.

Lacis, A. A., and J. E. Hansen, 1974: A parameterization for the absorption of solar radiation in the earth's atmosphere. *J. Atmos. Sci.,* **31,** 118–133.

Liou, K. N., 1973: Transfer of solar irradiance through cirrus cloud layers. *J. Geophys. Res.,* **78,** 1409–1418.

——, 1974: On the radiative properties of cirrus in the window region and their influence on remote sensing of the atmosphere. *J. Atmos. Sci.,* **31,** 522–532.

——, 1980: *An Introduction to Atmospheric Radiation.* Int. Geophys. Ser., Vol. 26., Academic Press, 392 pp.

——, 1986: Influence of cirrus clouds on weather and climate processes: A global perspective. *Mon. Wea. Rev.,* **114,** 1167–1199.

——, S. C. Ou, Y. Takano, F. P. J. Valero, and T. P. Ackerman, 1990: Remote sounding of the tropical cirrus cloud temperature and optical depth using 6.5 and 10.5 μm radiometers during STEP. *J. Appl. Meteor.,* **29,** 716–726.

Minnis, P., 1989: Viewing zenith angle dependence of cloudiness determined from coincident GOES East and GOES West data. *J. Geophys. Res.*, **94,** 2303–2320.

——, and E. F. Harrison, 1984: Diurnal variability of regional cloud and clear-sky radiative parameters derived from GOES data, Part I–III. *J. Climate Appl. Meteor.*, **23,** 993–1052.

——, and B. A. Wielicki, 1988: Comparison of cloud amounts derived using GOES and Landsat data. *J. Geophys. Res.*, **93,** 9385–9403.

——, E. F. Harrison, and G. G. Gibson, 1987: Cloud cover over the eastern equatorial Pacific derived from July 1983 ISCCP data using a hybrid bispectral threshold method. *J. Geophys. Res.*, **92,** 4051–4073.

——, P. W. Heck, and E. F. Harrison, 1990a: The 27–28 October 1986 FIRE IFO Cirrus Case Study: Cloud parameter fields derived from satellite and lidar data. *Mon. Wea. Rev.*, **118,** 2426–2446.

——, D. F. Young, K. Sassen, J. M. Alvarez, and C. J. Grund, 1990b: The 27–28 October 1986 FIRE IFO Cirrus Case Study: Cirrus parameter relationships derived from satellite and lidar data. *Mon. Wea. Rev.*, **118,** 2402–2425.

——, P. W. Heck, and D. F. Young, 1993: Inference of cirrus cloud properties using satellite-observed visible and infrared radiances. Part II: Verification of theoretical cirrus radiative properties. *J. Atmos. Sci.*, **50,** 1305–1322.

Paltridge, G. W., and C. M. R. Platt, 1981: Aircraft measurements of solar and infrared radiation and the microphysics of cirrus cloud. *Quart. J. Roy. Meteor. Soc.*, **107,** 367–380.

Platt, C. M. R., 1973: Lidar and radiometric observations of cirrus clouds. *J. Atmos. Sci.*, **30,** 1191–1204.

——, 1979: Remote sounding of high clouds, I: Calculations of visible and infrared optical properties from lidar and radiometer measurements. *J. Appl. Meteor.*, **18,** 1130–1143.

——, 1983: On the bispectral method for cloud parameter determination from satellite VISSR data: Separating broken cloud and semitransparent cloud. *J. Climate Appl. Meteor.*, **22,** 429–439.

——, and A. C. Dilley, 1979: Remote sounding of high clouds: II. Emissivity of cirrostratus. *J. Appl. Meteor.*, **18,** 1144–1150.

——, and G. L. Stephens, 1980: The interpretation of remotely sensed high cloud emittances. *J. Atmos. Sci.*, **37,** 2314–2322.

——, and A. C. Dilley, 1984: Determination of cirrus particle single-scattering phase function from lidar and solar radiometric data. *Appl. Opt.*, **23,** 380–386.

——, D. W. Reynolds, and N. L. Abshire, 1980: Satellite and lidar observations of the albedo, emittance, and optical depth of cirrus compared to model calculations. *Mon. Wea. Rev.*, **108,** 195–204.

——, J. C. Scott, and A. C. Dilley, 1987: Remote sounding of high clouds, VI. Optical properties of midlatitude and tropical cirrus. *J. Atmos. Sci.*, **44,** 729–747.

Reynolds, D. W., and T. H. Vonder Haar, 1977: A bispectral method for cloud parameter determination. *Mon. Wea. Rev.*, **105,** 446–457.

Roberts, R. E., J. E. A. Selby, and L. M. Biberman, 1976: Infrared continuum absorption by atmospheric water vapor in the 8–12 *um* window. *Appl. Opt.*, **15,** 2085–2090.

Rossow, W. B., L. C. Garder, P. Lu, and A. Walker, 1988: International Satellite Cloud Climatology Project (ISCCP), Documentation of cloud data. WCRP Rep., 78 pp.

Rothman, L. S., R. R. Gamache, A. Barbe, A. Goldman, J. R. Gille, L. R. Brown, R. A. Toth, J. M. Flaud, and C. Camy-Peyret, 1983: AFGL atmospheric absorption line parameters compilation: 1982 edition. *Appl. Opt.*, **22,** 2247–2256.

Schenk, W. E., and R. J. Curran, 1973: A multispectral method for estimating cirrus cloud top heights. *J. Appl. Meteor.*, **12,** 1213–1216.

Schiffer, R. A., and W. B. Rossow, 1983: The International Satellite Cloud Climatology Project (ISCCP): The first project of the World Climate Research Programme. *Bull. Amer. Meteor. Soc.*, **64,** 779–784.

Slingo, A., and J. M. Slingo, 1988: The response of a general circulation model to cloud longwave forcing. I: Introduction and initial experiments. *Quart. J. Roy. Meteor. Soc.*, **114,** 1027–1062.

Smith, W. L., H. M. Woolf, and W. J. Jacob, 1970: A regression method for obtaining real-time temperature and geopotential height profiles from satellite spectrometer measurements and its application to Nimbus 3 SIRS observations. *Mon. Wea. Rev.*, **98,** 604–611.

Starr, D. O'C., 1987: A cirrus-cloud experiment: Intensive field observations planned for FIRE. *Bull. Amer. Meteor. Soc.*, **68,** 119–124.

Stephens, G. L., 1980: Radiative properties of cirrus clouds in the infrared region. *J. Atmos. Sci.*, **37,** 435–446.

Suttles, J. T., R. N. Green, P. Minnis, G. L. Smith, W. F. Staylor, B. A. Wielicki, I. J. Walker, D. F. Young, V. R. Taylor, and L. L. Stowe, 1988: Angular radiation models for earth-atmosphere system. NASA RP-1184, 144 pp. [Available from R. N. Green or P. Minnis, MS 420, NASA Langley Research Center, Hampton, Virginia 23665-5225.]

Takano, Y., and K. N. Liou, 1989a: Radiative transfer in cirrus clouds: I. Single scattering and optical properties of oriented hexagonal ice crystals. *J. Atmos. Sci.*, **46,** 3–19.

——, and ——, 1989b: Radiative transfer in cirrus clouds: II. Theory and computation of multiple scattering in an anisotropic medium. *J. Atmos. Sci.*, **46,** 20–38.

Wielicki, B. A., and J. A. Coakley, Jr., 1981: Cloud retrieval using infrared sounder data: Error analysis. *J. Appl. Meteor.*, **20,** 157–169.

Wu, M. L., 1985: Remote sensing of cloud-top pressure using reflected solar radiation in the oxygen A-band. *J. Climate Appl. Meteor.*, **24,** 539–546.

Wylie, D. P., and W. P. Menzel, 1989: Two years of cloud cover statistics using VAS. *J. Climate,* **2,** 380–392.

Yeh, H. Y., and K. N. Liou, 1983: Remote sounding of cloud parameters from a combination of infrared and microwave channels. *J. Climate Appl. Meteor.*, **22,** 201–213.